Review Vol. 7, No. 2 / February 2019 / Photonics Research 121

PHOTONICS Research

Vertical-cavity surface-emitting lasers for data communication and sensing

Anjin Liu,[1,2,3,*] Philip Wolf,[4] James A. Lott,[4] and Dieter Bimberg[4,5]

[1]Laboratory of Solid-State Optoelectronics Information Technology, Institute of Semiconductors, Chinese Academy of Sciences, Beijing 100083, China
[2]State Key Laboratory on Integrated Optoelectronics, Institute of Semiconductors, Chinese Academy of Sciences, Beijing 100083, China
[3]Center of Materials Science and Optoelectronics Engineering, University of Chinese Academy of Sciences, Beijing 100049, China
[4]Institute of Solid State Physics and Center of Nanophotonics, Technische Universität Berlin, Hardenbergstrasse 36, 10623 Berlin, Germany
[5]Bimberg Chinese-German Center for Green Photonics of the Chinese Academy of Sciences at CIOMP, Changchun 130033, China
*Corresponding author: liuanjin@semi.ac.cn

Received 7 September 2018; accepted 27 November 2018; posted 30 November 2018 (Doc. ID 352384); published 9 January 2019

Vertical-cavity surface-emitting lasers (VCSELs) are the ideal optical sources for data communication and sensing. In data communication, large data rates combined with excellent energy efficiency and temperature stability have been achieved based on advanced device design and modulation formats. VCSELs are also promising sources for photonic integrated circuits due to their small footprint and low power consumption. Also, VCSELs are commonly used for a wide variety of applications in the consumer electronics market. These applications range from laser mice to three-dimensional (3D) sensing and imaging, including various 3D movement detections, such as gesture recognition or face recognition. Novel VCSEL types will include metastructures, exhibiting additional unique properties, of largest importance for next-generation data communication, sensing, and photonic integrated circuits.

https://doi.org/10.1364/PRJ.7.000121

1. INTRODUCTION

Semiconductor heterostructure lasers are key enabling devices in our Internet society governed by the science of light: photonics. Outstanding properties of such lasers are the high efficiency of the conversion of electrical energy to photons, the small footprint, the modulation bandwidth, the excellent reliability, and the low cost. Important applications include optical communication, optical storage, sensing, printing, pumping for other lasers, and micro-invasive surgery. The vertical-cavity surface-emitting laser (VCSEL) arose from the ideas and contributions of several research groups. The first semiconductor laser emitting perpendicular to the surface of a semiconductor wafer traces back to the work of Melngailis in Ref. [1]. A surface-emitting laser diode on an InP substrate with a 90 μm long cavity and planar metal mirrors that operated at 77 K was demonstrated by Soda *et al.*, which is often recognized as the inspiration for what is now known as a VCSEL [2]. Since this early publication on a surface-emitting laser diode, which is separate from the idea of using a grating to produce lasing perpendicular to the wafer surface for a conventional horizontal Fabry–Perot cavity, numerous research groups have contributed to the evolution and improvement of the device we now call a VCSEL, including the seminal idea of using semiconductor distributed Bragg reflectors (DBRs) as mirrors [3,4], the use of a DBR to form a surface-emitting laser [5–8], the use of quantum wells (QWs) placed at optical field intensity antinodes in the optical cavity [9–13], and the use of oxide apertures [14–17]. Many other significant and pioneering contributions on VCSELs, VCSEL arrays, and VCSEL applications were made by many research groups from the 1980s to the present [18–29]. These contributions are far too numerous to list or adequately describe in detail here. We nonetheless pay tribute to those distinguished researchers who led the epic journey of the VCSEL from the 1960s to the present day. Significant advances in epitaxial growth and device processing schemes circa the 1980s to the present have also contributed significantly to the advancement of VCSELs.

A modern VCSEL is constructed by two DBRs aligned in the vertical direction to form a vertical laser cavity, and the light output is along the same vertical wafer epitaxial growth direction normal to the wafer. Such a unique device structure is very different from an edge-emitting laser, which endows a VCSEL with many notable advantages and performance attributes as compared to other types of laser diodes. The small cavity volume brings a low threshold current, high quantum efficiency, and high-speed modulation at a low current. The symmetric transverse structure and surface emission of a VCSEL lead to a circular and non-astigmatic beam, good for coupling to an optical fiber and other optics. Surface emission also enables a large-scale two-dimensional (2D) VCSEL array and

wafer level fabrication and testing for an overall low cost of manufacturing.

VCSELs have experienced exponential growth in key photonics application areas, for example, in data communication, optical sensing, laser printing, light detection and ranging (LiDAR), and illumination, to mention a few [18–29]. In this paper, we will focus on GaAs-based VCSELs for data communication and sensing that emit at 850–1000 nm. Our overview in Section 2 is applicable to InP-based and GaN-based VCSELs as described in, for example, Refs. [30–33].

2. FUNDAMENTALS OF VCSELs

A. Structure of VCSELs

The modern VCSEL is constructed by combining a gain region within an optical cavity with two highly reflective DBRs to form a vertical resonator, as shown in Fig. 1. The gain region is predominantly a set of one or more QWs or sheets of quantum dots that are bunched together and positioned at the central antinode of the standing wave on resonance of the vertical resonator to provide efficient optical amplification. The DBRs are composed of alternating layers of high and low refractive index materials, where the optical thickness of each layer is a quarter-wavelength. The DBR mirror attains a power reflectance (R) of 0.99 or larger at the resonant design wavelength. The top and bottom metal contacts inject current into the central active gain region. Oxide apertures are formed by the selective thermal oxidation of Al-rich AlGaAs layers. These oxide layers, which are typically 20–30 nm in thickness, confine the current and, at the same time, guide the optical field intensity within the VCSEL. The use of oxide apertures can effectively reduce the optical losses, reduce the threshold current, and enhance the VCSEL's power conversion efficiency. The output light can be emitted by a top coupling DBR when the DBR's R is made to be below 0.999, while the R of the bottom DBR mirror is made to be near 1.0. In general, the coupling DBR mirror has an R at the emission wavelength between about 0.98 and 0.999. Alternatively, the R of the top DBR may be set close to 1.0 by increasing the number of DBR periods, while the R of the bottom DBR is set to below 0.999 so the VCSEL emission may be directed downward through the substrate and out into free space (usually into the air). In this scenario, ideally it is desirable that the substrate is transparent to the lasing wavelength, and thus the power absorptance of the bottom DBR is zero.

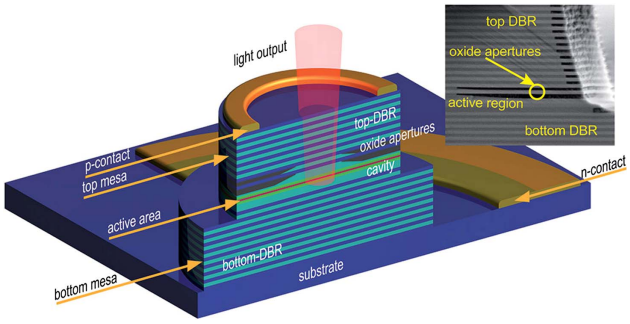

Fig. 1. Schematic of a top-emitting VCSEL [19]. Inset is a scanning electron microscope image of the cross section of a high-speed VCSEL after it is cleaved.

B. Dynamics of VCSELs

Figure 2 illustrates a small-signal model of a VCSEL together with the high-frequency driving source, consisting of a voltage source v_s and a characteristic impedance Z_0. The dynamical behavior of semiconductor lasers can be described using a rate equation model [34]. The modulation rate of a VCSEL is limited by the intrinsic damping, self-heating effects, and electrical parasitics. The intrinsic modulation response of a semiconductor laser can be expressed by the transfer function [34]

$$H_{\text{in}}(f) = A \times \frac{f_r^2}{f_r^2 - f^2 + i\frac{f}{2\pi}\gamma}, \tag{1}$$

where A is a constant, f_r is the relaxation resonance frequency, i is the imaginary unit, and γ is the damping factor.

The relaxation resonance frequency is an oscillation frequency between the carriers and photons that interact via stimulated emission in the laser cavity. The relaxation resonance frequency increases with the square root of the bias current and is formulated as

$$f_r = D\sqrt{I - I_{\text{th}}}, \tag{2}$$

where the D-factor is

$$D = \frac{1}{2\pi}\sqrt{\frac{\eta_i \Gamma v_g}{qV_a} \times \frac{\partial g/\partial n}{\chi}}, \tag{3}$$

and where I_{th} is the threshold current, Γ is the optical confinement factor, η_i is the internal quantum efficiency, v_g is the photon group velocity, V_a is the volume of the active region, $\partial g/\partial n$ is the differential gain, and χ is the transport factor.

The damping factor γ limits the laser diode's achievable bandwidth jointly with the relaxation resonance frequency, leading to a flatter frequency response as γ increases. The frequency response is a generally desired advantage of VCSELs for data transmission since this may improve the optical eye opening and thus the achievable error-free bit rate. The damping factor increases with an increase of the relaxation resonance frequency as given in the following equation:

$$\gamma = Kf_r^2 + \gamma_0, \tag{4}$$

where the K-factor is

$$K = 4\pi^2\left(\tau_p + \frac{\varepsilon\chi}{v_g \partial g/\partial n}\right), \tag{5}$$

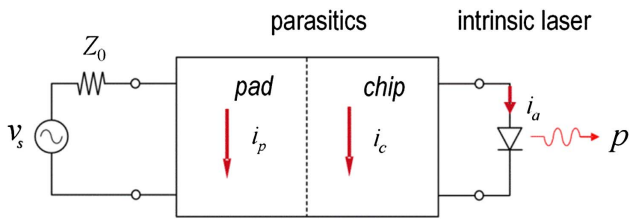

Fig. 2. Small-signal model of a VCSEL with the high-frequency driving source.

τ_p is the photon lifetime, and ε is the gain compression factor. The damping offset γ_0 is inversely proportional to the differential carrier lifetime.

To achieve a high modulation bandwidth, a large D-factor and a reasonably low K-factor are preferred, i.e., we seek a high differential gain using strained QWs [35–37], a low photon lifetime by tuning the phase of the top DBR [38,39], and a high confinement factor by employing a short cavity and a small oxide aperture [40–42]. In reality, the relaxation resonance frequency and damping factor do not linearly increase with $\sqrt{I - I_{\text{th}}}$ and f_r^2, respectively, because of thermal effects and additional loss mechanisms that occur at high currents [20]. The thermal effects in high-speed VCSELs can be relieved by reducing the series resistance of the VCSEL [43], using DBRs with a high thermal conductivity [44,45], employing copper-plated heat sinks [46], and bonding VCSEL chips to efficient heat sinks [47].

Electrical parasitics including bonding pads eventually limit the modulation bandwidth of a VCSEL. The transfer function introduced by electrical parasitics can be expressed by a single-pole low-pass filter transfer function as

$$H_p(f) = B \times \frac{1}{1 + i(f/f_p)}, \tag{6}$$

where B is a constant, and f_p is the parasitic cutoff frequency. The parasitic resistances are mainly contributed by the series resistance of the DBRs, the junction resistance, and a resistance due to the oxide apertures. The parasitic capacitances arise primarily from the intrinsic diode junction, one or more oxide layers, the area of the mesa containing the aperture, and the metal contact pads. To reduce parasitic resistances, modifications of conduction and valence band interfaces in DBRs and modulated doping profiles are adopted while keeping any absorption loss to a minimum [48]. Thick insulating materials like polyimide and benzocyclobutene (BCB) with a low dielectric constant underneath the signal pad are used to planarize the mesa and reduce the pad capacitance [49,50]. Multiple deep oxidation layers and proton implantation are also employed to reduce the mesa capacitance [51–53].

The overall electrical small-signal modulation response of a VCSEL is given by multiplying the intrinsic transfer function with the transfer function introduced by the electrical parasitics, and thus

$$\begin{aligned} H(f) &= H_{\text{in}}(f) \times H_p(f) \\ &= C \times \frac{f_r^2}{f_r^2 - f^2 + i\frac{f}{2\pi}\gamma} \times \frac{1}{1 + i\left(\frac{f}{f_p}\right)}, \end{aligned} \tag{7}$$

where C is a constant [34].

3. VCSELs FOR DATA COMMUNICATION

VCSELs are the dominant optical sources for multimode fiber (MMF)-based optical links in data centers and high-performance computers (HPCs). Since the network traffic exponentially increases year by year, wide modulation bandwidth is an essential requirement to meet the thirst for ever higher transmission data rates, and more and more power in data centers and HPCs is consumed. The heat dissipated leads to an operating environment reaching temperatures of 85°C, even with advanced cooling technologies. The latest communication system designs seek to develop VCSELs that are more energy efficient and that are capable of maintaining their room temperature modulation bit rates at high temperatures without adjusting the operating parameters.

A. Modulation Speeds of VCSELs

Table 1 lists some typically reported modulation bandwidths and error-free bit rates of VCSELs via the standard on–off

Table 1. Modulation Bandwidths and Bit Rates of VCSELs at Room Temperature Using the Standard On–Off Keying in a Back-to-Back Data Transmission Configuration

Group	λ (nm)	Bandwidth (GHz)	Bit Rate (Gbps)	Temperature (°C)	Oxide Aperture (μm)	Year	Refs.
IBM	850	15.4	20	25	8	2001	[54]
Finisar-IBM	850	19	30	25	6	2008	[55]
CUT	850	20	32	25	9	2009	[56]
CUT	850	23	40	25	7	2010	[57]
CUT	850	28	44	25	7	2012	[58]
CUT	850	24	57	25	8	2013	[59]
CUT	850	30	50	25	3.5	2015	[60]
TU Berlin	850	20	30	25	6	2009	[61]
TU Berlin	850		40	25	9	2009	[62]
UIUC	850	21.2	40	20	4	2014	[63]
UIUC	850	29.2	57	25	5	2016	[64]
NCU	850	22.4	40	25	4	2013	[65]
NCU	850	26	41	25	8	2015	[66]
UCSB	980	>20	35	20	3	2007	[67]
TU Berlin	980		44	25	6	2011	[40]
TU Berlin	980	24.7	50	25	5	2014	[68]
TU Berlin	980	26.6	52	25	6	2016	[39]
TU Berlin	980	35.5		25	3	2018	[69]
CUT	1060	22	50	25	4	2017	[70]
NEC	1100	20	25	25	6.9	2006	[53]
NEC	1100	24	30	25	6	2007	[71]
NEC	1100	24	40	25	6	2008	[72]

keying modulation format in a back-to-back measurement configuration from the past decade. The error-free bit rates are determined from transmission tests where the reported bit error ratio (BER) is $<10^{-12}$. The 850 nm wavelength is presently the standard for data communication based on systems using the standard OM3, OM4, or the new OM5 MMFs. Initially, conventional 850 nm VCSELs employed unstrained GaAs QWs with AlGaAs as the barrier layers. The highest data rate of 30 Gbps at 25°C was reported for a 6 μm oxide aperture diameter VCSEL with GaAs QWs in 2008 [55]. InGaAs QWs have a larger differential gain compared to unstrained GaAs QWs and are adopted for contemporary high-speed VCSELs for emission at or near 850 nm [36,37]. In 2009, error-free data transmission of 32 Gbps at 25°C was achieved with InGaAs QWs and double oxide layers by Chalmers University of Technology (CUT) [56]. An error-free transmission rate of 39 Gbps and open-eye operation at 40 Gbps at 25°C were reported in the same year by Technische Universität (TU) Berlin [62]. In 2012, CUT demonstrated a high-speed VCSEL with 44 Gbps error-free transmission and a modulation bandwidth of 28 GHz at 25°C [58]. This result was achieved by using a half-wavelength cavity for improved transport and a larger longitudinal optical confinement, adding four $Al_{0.96}Ga_{0.04}As$ layers to reduce parasitics and tuning the photon lifetime by shallow surface etching. Later, error-free transmission of 57 Gbps in a VCSEL with a 3 dB bandwidth of 24 GHz at 25°C was reported [59]. This error-free transmission rate was pushed to 71 Gbps with two-tap feed-forward equalization in a collaboration between CUT and International Business Machines (IBM) Corporation [73]. A modulation bandwidth of 30 GHz was reached for a 3.5 μm oxide aperture diameter VCSEL by using a half-wavelength cavity, four deep oxide layers, tuning photon lifetime, and one oxide aperture at both the n- and p-DBR sides of the optical cavity [60,74].

Other groups also reported many exciting results on high-speed VCSELs in the 850 nm range. IBM and Finisar jointly reported a 55 Gbps directly modulated 850 nm VCSEL-based optical link in 2012 and a 56.1 Gbps link in 2013 [75,76]. Shi *et al.* reported a VCSEL with an open-eye operation at 41 Gbps at 25°C in 2015 [66]. This group used an oxide relief structure to reduce parasitics and Zn diffusion to define the optical aperture to a narrow spectral width and to reduce the differential resistance. In 2016, a University of Illinois Urbana-Champaign (UIUC) group reported a high-speed 850 nm VCSEL with error-free transmission at 50 Gbps and a 3 dB modulation bandwidth of 28.2 GHz [77].

VCSELs emitting at or in the range 980 to 1100 nm are now becoming important for data communication, most especially for wavelength division multiplexing and free-space optical communication [78]. Compared with the 850 nm wavelength range, in particular the 980 and 1100 nm wavelength ranges benefit from a larger temperature insensitivity, lower chromatic dispersion and lower transmission loss in the standard OM3 and OM4 MMF, a higher sensitivity of the photodetectors, and increased eye safety. InGaAs QWs emitting at 980 or 1100 nm exhibit a larger differential gain and lower transparency carrier density, promising a higher conversion efficiency, lower threshold current, higher modulation bandwidth, and higher reliability.

In 2007, error-free operation at 35 Gbps was demonstrated with a 980 nm VCSEL by the Coldren group at the University of California Santa Barbara (UCSB). This VCSEL used a tapered oxide aperture to reduce optical loss, multiple deep oxide layers to reduce the parasitic capacitance, and an optimized p-doping profile in the top DBRs to lower the loss and the resistance, showing a 3 dB modulation bandwidth larger than 20 GHz [50]. In 2011, TU Berlin demonstrated a 980 nm VCSEL realizing error-free transmission up to 44 Gbps at 25°C by shortening the cavity length to half-wavelength, using modulation doping and a binary DBR [40,79]. 980 nm VCSELs with 50 Gbps error-free transmission and 3 dB modulation bandwidth of about 27 GHz were demonstrated at 25°C by using a half-wavelength-thick optical cavity, tuning the VCSEL's photon lifetime, and including current spreading layers [39,68,80]. In 2017, TU Berlin reported the simplicity VCSEL that employs a simplified epitaxial layer design with a 3 dB small-signal modulation bandwidth of 31–34 GHz [81,82]. This 1.5–2.5 μm oxide aperture VCSEL has a half-wavelength cavity and one oxide aperture at both the n- and p-DBR sides of the optical cavity for strong optical field and carrier confinements but without any deep oxide layers. Such a simple VCSEL structure is expected to improve the reliability and might ease manufacturing of large-diameter VCSEL wafers of 101.6 mm diameter or larger. In 2018 the same TU Berlin group reported a new record bandwidth of 35.5 GHz with their 980 nm VCSELs [69].

For VCSELs emitting at or near 1100 nm, Nippon Electric Company Ltd. (NEC) demonstrated error-free 25 Gbps operation at 25°C and a 3 dB modulation bandwidth up to 20 GHz in 2006 [83]. A 3 dB modulation bandwidth of 24 GHz was achieved with error-free operations at 30 Gbps and later 40 Gbps using buried type-II tunnel junctions [71,72].

Currently, over 90% of the MMF links are less than 100 m [84]. As the data centers become permanently larger, longer reach optical links up to ~2 km at 20–25 Gbps are desirable [85]. Due to modal dispersion, it is challenging to realize error-free transmission at 20–25 Gbps across 2 km with a multi-mode VCSEL. To take care of the modal dispersion, VCSELs with a high side mode suppression ratio (a reduced spectral width) are sought for the long-distance transmission. The direct approach for VCSELs with a reduced spectral width is to reduce the oxide aperture. In 2013, TU Berlin reported 25 Gbps transmission across 1 km of OM4 MMF with a 3 μm oxide aperture VCSEL at 850 nm [86]. CUT used the surface relief method to control the modes and reported 20 Gbps transmission across 2 km of OM4 MMF with a 6 μm oxide aperture together with a 3 μm optical aperture VCSEL at 850 nm in 2014 [87]. Surface relief VCSELs show a lower current density than VCSELs with a reduced oxide aperture, demanding a more complicated fabrication and an increased threshold current.

Efforts have also been carried out to explore unconventional VCSELs with transverse coupled cavities for additional photon–photon resonances to extend the modulation bandwidth [88,89]. Such VCSELs demonstrated a 3 dB modulation bandwidth up to 37 GHz. The 3 dB modulation bandwidth of these VCSELs is very sensitive to the coupling strength between the

cavities and the phase of the feedback light. The out-of-phase feedback is reportedly beneficial to extend the modulation bandwidth.

B. High-Temperature VCSELs

The ambient temperature can reach 85°C in data centers and HPCs, even with advanced cooling technology. Such a temperature might deteriorate the performance (data rate, energy consumption, reliability). VCSELs can maintain the room temperature performance without adjusting driving conditions and adding extra cooling systems by detuning the laser cavity resonance from the gain peak [90]. The gain peak of QWs shifts faster to larger wavelengths than the cavity resonance as temperature increases due, for example, to increasing bias current via joule heating. Therefore, as shown in Fig. 3, the cavity resonance is typically designed to be at room temperature at the longer wavelength side of the gain peak. When increasing the temperature, the gain peak and the cavity resonance wavelength will align, and the threshold current might decrease instead of increasing. The performance of various VCSEL designs at high temperatures in an on–off keying modulation format and measured in a back-to-back configuration is summarized in Table 2. Finisar reported 850 nm devices operating at 14 Gbps at 95°C in 2012 [91]. In 2013 Sumitomo described 850 nm VCSELs operating at 28 Gbps at 85°C [92]. Also, in 2013 CUT presented an 850 nm VCSEL operating at 40 Gbps at 85°C [93] and together with IBM in 2015 reached 50 Gbps at 90°C [94]. In 2016, UIUC reported an 850 nm VCSEL at 85°C [64] with an error-free data rate of 50 Gbps. VIS reported in 2018 a data rate of 25 Gbps at 150°C for their 850 nm VCSEL with a gain-to-cavity detuning of ~15 nm [95]. For 980 nm VCSELs, TU Berlin reported error-free transmission at 30 Gbps at 120°C in 2011 [40] and 46 Gbps at 85°C in 2014 [68]. These results were exceeded in 2016 with 50 Gbps at 85°C for a 980 nm VCSEL [39]. For 1060 nm VCSELs, Chalmers reported a data rate of 40 Gbps at 85°C [70].

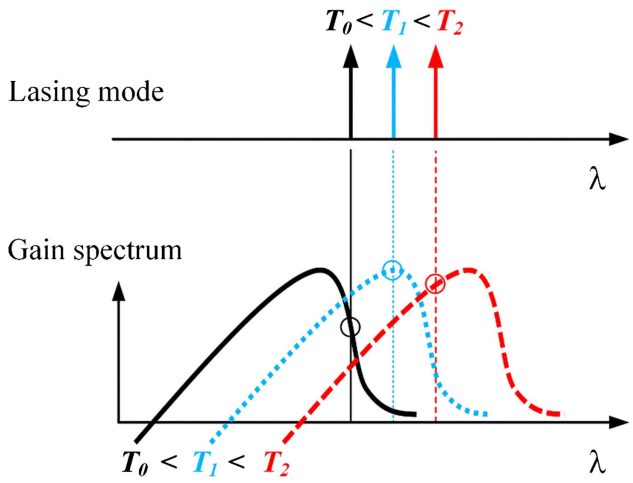

Fig. 3. Schematic of representative optical modes (straight lines) and gain spectra (curves) behavior in a VCSEL as functions of increasing temperature. T_0 denotes the typical room temperature.

C. Energy Efficiency of VCSELs

Power consumption becomes more and more important for both data centers and HPCs. Large power consumption increases the economic and ecological cost. Large power consumption might also deteriorate the long-term stability of VCSELs. The energy-to-data rate ratio EDR $= (I \cdot V)/\mathrm{BR}$ (in fJ/bit or mW/Tbps) is used to compare the energy consumption of different VCSELs, where V and I are the bias voltage (V) and current (mA), and BR (Gbps) is the bit rate at error-free operation [96]. Energy efficiency is commonly also quantified by the dissipated heat-to-bit rate ratio (HBR), $\mathrm{HBR} = (I \cdot V - P_{\mathrm{opt}})/\mathrm{BR}$, where P_{opt} (milliwatt, mW) is the optical output power of the VCSEL [96]. According to the International Technology Roadmap for Semiconductors projections for 2022, less than 100 fJ/bit is required for off-chip

Table 2. Selected Results on Bandwidths and Bit Rates of VCSELs at High Temperatures in an On–Off Keying Modulation Format for Back-to-Back Data Transmission Configuration

Group	λ (nm)	Bandwidth (GHz)	Bit Rate (Gbps)	Temperature (°C)	Oxide Aperture (μm)	Year	Refs.
Finisar	850	10	14	95	8	2012	[91]
Emcore	850	16	28	85	7.5	2013	[92]
CUT	850	21	40	85	7	2013	[93]
IBM-CUT[a]	850	21	50	90	6	2015	[94]
UIUC	850	24.5	50	85	5	2016	[64]
NCU	850	22.4	34	85	4	2013	[65]
NCU	850	20	41	85	8	2015	[66]
VIS	850		25	150	4	2018	[95]
VIS	850		25	130	4	2018	[95]
TU Berlin	980	11	20	120	3	2008	[97]
TU Berlin	980		38	85	6	2011	[40]
TU Berlin	980		30	120	6	2011	[40]
TU Berlin	980	23	46	85	5	2014	[68]
TU Berlin	980		38	85	5.5	2014	[98]
TU Berlin	980	18	35	85	3	2014	[99]
TU Berlin	980	24.5	50	85	6	2016	[39]
CUT	1060	16	40	85	4	2017	[70]

[a]With tap feed forward equalization driver.

Table 3. Energy Efficiencies of High-Speed VCSELs with the On–Off Keying Modulation Format in a Back-to-Back Data Transmission Configuration

Group	λ (nm)	Bit Rate (Gbps)	Temperature (°C)	Energy eff. (fJ/bit)	Oxide Aperture (μm)	Year	Refs.
TU Berlin-VIS	850	25	25	99	2	2011	[96]
TU Berlin-VIS	850	17	25	69	2	2011	[96]
TU Berlin-VIS	850	25	25	56	3.5	2012	[101]
TU Berlin	850	40	25	108	4	2013	[104]
CUT	850	50	25	95	3.5	2015	[60]
CUT	850	40	25	73	3.5	2015	[60]
UIUC	850	40	20	395	4	2014	[63]
NCU	850	12.5	25	109	6	2011	[105]
NCU	850	34	25	345	6	2011	[105]
NCU	850	34	25	107	4	2013	[65]
UCSB	980	35	20	286	3	2009	[67]
TU Berlin	980	38	85	177	5.5	2014	[98]
TU Berlin	980	35	85	139	3	2014	[99]
TU Berlin	980	35	25	145	3	2015	[106]
Furukawa	1060	10	25	140		2011	[107]
Furukawa	1060	25	25	76		2014	[108]
CUT	1060	50	25	100	4	2017	[70]

optical interconnects, and 10 fJ/bit is required for on-chip optical interconnects [100].

Large energy efficiency was reported for small oxide aperture diameter VCSELs [101–103]. The main reason is the larger *D*-factor originating from the smaller mode volume of small aperture diameter VCSELs, while the damping (*K*-factor) is more or less independent of the aperture size. Thus, a larger −3 dB bandwidth at a smaller bias is realized. Table 3 summarizes the state of the art for energy-efficient high-speed VCSELs in an on–off keying modulation format for back-to-back data transmission at 850, 980, and 1060 nm. For 850 nm VCSELs, a record energy efficiency of 56 fJ/bit was achieved at 25 Gbps at 25°C for a 3.5 μm oxide aperture diameter VCSEL by TU Berlin and VIS in 2012 [101]. 145 fJ/bit at 35 Gbps at 25°C and 139 fJ/bit at 35 Gbps at 85°C were reported for a 980 nm 3 μm oxide aperture VCSEL by TU Berlin [98,106]. In 2014, Furukawa reported 76 fJ/bit at 25 Gbps at 25°C [108].

D. VCSELs with PAM4 Modulation Format

Today, short-reach optical interconnects are dominated by VCSELs combined with MMF and direct detection, offering low cost and small form factor. Existing IEEE standards (802.3bm) support 10 Gbps and 25 Gbps core rates in 4-fiber and 10-fiber arrangements to support up to 100 Gbps of traffic. However, a 400 GbE (Gigabit Ethernet supporting 400 Gbps) solution as envisioned by the IEEE Task Force (P802.3bs) based on 25 Gbps will require 16 fibers in each direction. Alternative solutions that lead to reduced fiber numbers could include higher bit rates combined with higher modulation formats to end up at 50+ Gbps per line. Four-level pulse amplitude modulation (PAM4) [109,110] is the presently most popular approach for higher-order modulation formats. Forward error correction and signal processing might help to surmount the 50 Gbps barrier reached by simple on–off keying.

Combining PAM4 and digital signal processing (DSP) techniques with coarse wavelength division multiplexing (CWDM, O-band) or short wavelength division multiplexing (SWDM) is enabling the next generation of high-speed optical VCSEL-based interconnects. Compared to the on–off keying modulation format, PAM is a way to transmit more bits into the same amount of time on a serial channel by using different signaling levels, as shown in Fig. 4. PAM4 has four distinct levels to encode two bits of data per symbol, essentially doubling the data rate of a connection. Generating or decoding more than two logical levels is technically more difficult, requiring more complex hardware and software and is probably energy inefficient. Already for PAM4, the VCSEL linearity, modulation response characteristics, and random and induced noise have become significant factors [111].

Recently, up to 94 Gbps PAM4 was demonstrated over single wavelengths using 850 nm VCSELs with a 20 GHz

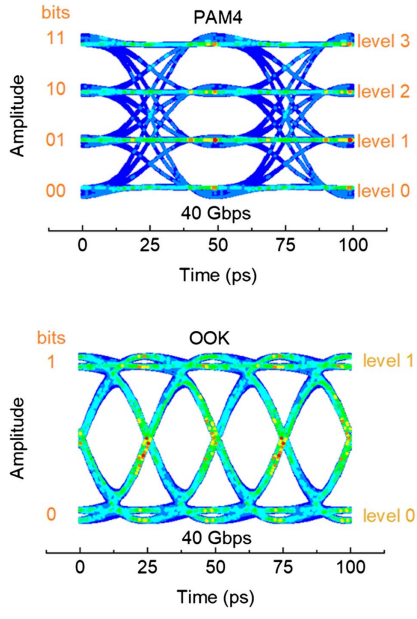

Fig. 4. Simulated PAM4 and on–off keying (OOK) eye diagrams at 40 Gbps with a constant modulation bandwidth of 20 GHz.

3 dB bandwidth using energy expensive pre-emphasis and receiver equalization [112]. 180 Gbps PAM4 was demonstrated using four VCSELs and short wavelength division multiplexing [113]. 38 Gbps PAM4 data transmission was successfully realized using 1.3 μm wafer-fusion VCSELs, a wavelength that is important for silicon photonics [111]. To continue using the present OM3 and OM4 MMF infrastructure SWDM is one promising approach to reduce fiber counts and cabling density and save substantial capital and operational cost [114].

E. VCSELs for Photonic Integrated Circuits

VCSELs are ideal sources for photonic integrated circuits (PICs). However, a VCSEL emits perpendicular to the wafer plane, while a PIC lies in the wafer plane. There are at least four approaches for coupling light from VCSELs to an in-plane PIC, as shown in Fig. 5. The most straightforward and direct approach is to use end-to-end coupling by placing a VCSEL at the end of an in-plane waveguide [115]. A spot-size converter is constructed to reduce the coupling loss between the VCSEL and an in-plane waveguide. The second approach is to use a 45° micro-reflector to direct the normally incident light from a VCSEL sitting on the top surface of a waveguide to an in-plane waveguide. A 45° micro-reflector can be fabricated mechanically or by etching, but the coupling efficiency is a very critical issue [116–119]. The third approach is based on a grating coupler. A buried diffraction grating is inserted in the top DBR of a GaAs-based VCSEL to couple the light into a horizontal waveguide [120]. This monolithic technology needs epitaxial regrowth. A more straightforward approach is to etch a surface grating into the top layer of the top DBR of a VCSEL needing no epitaxial regrowth. Such surface gratings achieved a coupling efficiency of 40% [121]. Recently, silicon grating couplers couple the light from VCSELs into the waveguide, showing 20 Gbps non-return to zero (NRZ) transmission at 1550 nm for packaged PICs [122–125]. The fourth approach is to use photonic wire bonding technology to connect a VCSEL to an in-plane waveguide [126]. The emerging photonic wire bonding technology has been used for chip-to-chip interconnects and chip-to-fiber interconnects. Very recently, hybrid integration of silicon photonics circuits and InP-based horizontal-cavity surface-emitting lasers by photonic wire bonding was demonstrated [127], which shows that the photonic wire bonding technology is a promising approach to realize the integration between a VCSEL and a PIC.

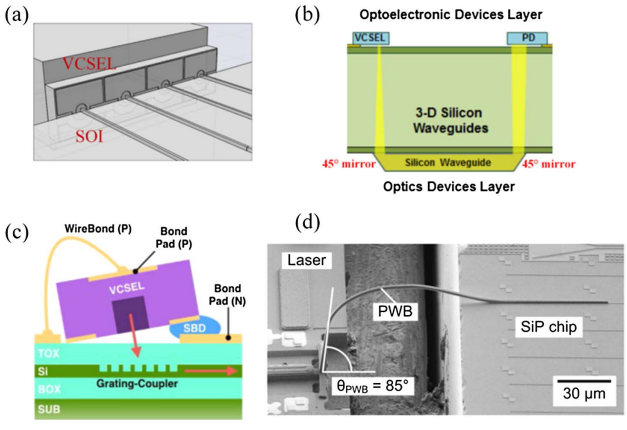

Fig. 5. (a) End-to-end coupling between a VCSEL and a PIC based on an SOI platform [115]. A spot-size convertor in the PIC side is always adopted for a high coupling efficiency between the VCSEL and the silicon waveguide. (b) VCSEL coupled to a PIC by 45° micro-reflectors [116]. (c) Grating coupler for coupling between a VCSEL and a PIC [123]. (d) Photonic wire bond for integration for a surface-emitting laser and a PIC [127]. The laser can be a VCSEL or a distributed-feedback surface-emitting laser. PWB, photonic wire bond.

4. VCSELs FOR SENSING

VCSELs show superior beam quality, low energy consumption, low cost, high reliability, and can be easily integrated to form 2D arrays, all requirements for sensing applications like mice or smartphones.

A. VCSEL-Based Sensors with Self-Mixing Interferometry

VCSELs used in optical mice first appeared in 2000 [22]. The tracking system in an optical mouse is based on the principle of laser self-mixing interference (SMI) [128–130]. As shown in Fig. 6, when the laser light emits to a scattering object, a small part of the scattered light is coupled back into the laser cavity and mixes with the strong laser field. When the movement of the object has a component along the direction of the laser beam, the phase of the reflected light continuously shifts with respect to the original laser light, resulting in a periodic variation of the feedback into the laser cavity at a frequency equal to the Doppler frequency [130]. The VCSEL is here used not only as a coherent light source but also an active filter, an amplifier, and an optical mixer. VCSELs with a small oxide aperture operate in a single mode, showing a high side mode suppression ratio (SMSR) at a very low threshold current and low power consumption, especially important for battery-powered optical mice. Large SMSRs in SMI sensors avoid signal distortion by mode beatings. The low output power of single-mode devices is acceptable for consumer electronics where the eye safety limit is 0.5 mW [21]. However, small oxide apertures of 3 μm are challenging for fabrication with high yield [131]. Next-generation tracking systems require single-mode and single-polarization VCSELs to avoid unwanted movement of the pointer due to polarization flips [132]. Many approaches have been proposed to break the radial symmetry of a typical vertical cavity laser. These approaches include the use of one-dimensional (1D) gratings [133,134], photonic

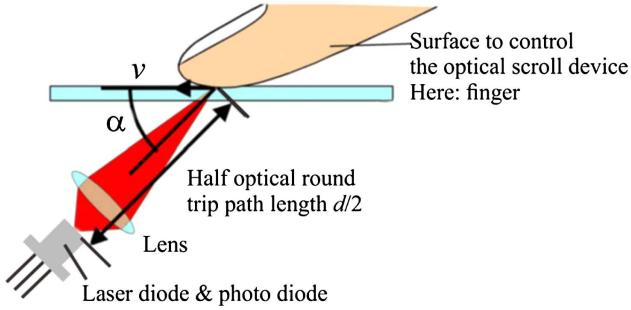

Fig. 6. Schematic of a tracking system based on SMI [129,130].

crystals [135,136], and elliptical surface etching [137]. Other approaches are based on the epitaxial growth on higher-order substrates [138,139], highly strained QWs [140], elliptically shaped mesa geometries [141,142], and the use of external stress [143].

VCSEL-based sensors based on SMI have many industrial applications in, e.g., cable manufacturing; extrusion; steel, paper processing and other production equipment; and in measuring length and movements of objects [144]. These sensors measure the true object speed and displacement on virtually all surfaces and have a high speed and displacement accuracy outperforming currently available sensors. VCSEL-based sensors with the SMI effect also have a vast potential to measure the speed over the ground of cars with high accuracy on all surfaces and under all automotive conditions (e.g., rain, fog, snow) instead of measuring the wheel speed [144]. Thus, they are also useful in braking distance reduction, lip control, side-wind correction, parking assistance, and tire monitoring.

B. VCSEL-Based Sensors for Three-Dimensional Sensing

VCSELs have considerable potential in three-dimensional (3D) sensing, such as in gesture recognition, face recognition, eye movement tracking, as well as in 3D photography and autofocusing [26,145]. The incorporation of VCSEL chips in smartphones is nowadays a reality [23].

For 3D sensing applications, VCSELs have huge advantages as compared to competing approaches. VCSELs emit with a narrow spectral width of less than 1 nm, which is much lower than the emission width of LEDs, and have a temperature dependence of typically 0.06 nm/K [146]. This allows the use of narrowband filters to eliminate unwanted background signals and enhance the signal-to-noise ratio, which is a prerequisite for many outdoor sensing applications. The circular output beam with a low divergence angle and the configurability of large-scale arrays result in scalable output power and an efficient and easy beam combination with simple optics making modules very compact. VCSELs are surface mountable, and have a wide variety of packaging options, including a chip on board, surface mount, and plastic encapsulation. They can be easily integrated with other electronic components on a printed circuit board (PCB). This packaging approach can reduce the cost and improve the VCSEL-based module performance by minimizing parasitics. VCSELs have high power conversion efficiencies of typically >40% across a wide temperature range from 0 to 70°C with superior performance [26].

There are primarily two types of methods for 3D sensing. The first one is the time-of-flight (ToF) method [147,148]. The ToF VCSEL chip of modern smartphones is shown in Fig. 7(a). A pulsed ToF system (also called a LiDAR system) sends a laser pulse to the object and measures the time that the light pulse travels from the laser to the object and back to the detector, yielding the 3D position (or depth information). The peak power of VCSELs (or a VCSEL array) depends on the pulse duration, the duty cycle, and also the thermal operating condition. These three factors also contribute to the power conversion efficiency. Self-heating in a VCSEL leading to thermal roll-over limits the peak optical output power. Short pulses, shorter than the thermal time constant (typically about

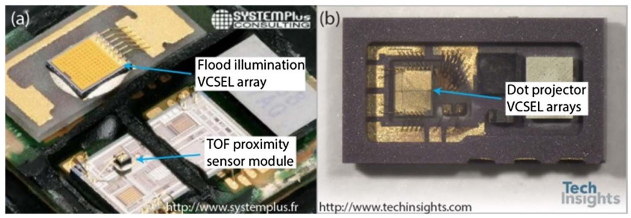

Fig. 7. Components of a face recognition module in a modern smartphone. (a) VCSELs for time-of-flight (ToF) proximity sensing and IR illumination. (b) VCSEL array for projection of randomly distributed dots to sense object distance information.

1 μs), with a small enough duty cycle can eliminate this limitation. In 3D sensing, human eye safety is another critical issue that must be carefully addressed [149].

The first ToF technology for 3D sensing is called a scanning ToF sensor, where single pixels are scanned one at a time with a VCSEL via short pulses. In a scanning ToF sensor, the pulse duration is always 1–10 ns, and the duty cycle is less than 10% [26,145,149,150]. VCSELs for such outdoor applications require a large optical output power for covering larger distances and still achieving a large signal-to-noise ratio [144]. The second technology is based on a ToF camera and is called focal plane scanning [148,151,152]. In such a sensing system, as shown in Fig. 8(a), VCSELs and detector arrays are used. Focal plane scanning uses a beam from the laser array to illuminate the complete field of view on a surface. Each detector covers its own fraction of the field of view, which is illuminated by the VCSEL array. Detector signals are analyzed in the time domain, and the distance to particular points of the target is determined on the basis of time-interval measurements. The VCSEL array should show low coherence and high optical power but lower brightness as compared to the scanning ToF sensor. VCSELs have the intrinsic advantage in that they may easily be produced in the form of 2D electrically parallel arrays [152].

An alternative method for 3D sensing uses structured light [26,153]. As shown in Fig. 8(b), here a coded 2D pattern generated by a special projector or a light source modulated by a spatial light modulator illuminates a surface. An imaging sensor is used to acquire a 2D image. A VCSEL array for generating the pattern is shown in Fig. 7(b). If the surface is nonplanar, the image of the surface from the camera is distorted compared to the coded 2D pattern. The depth information can be extracted from the distortion of the known coded 2D pattern. The coded

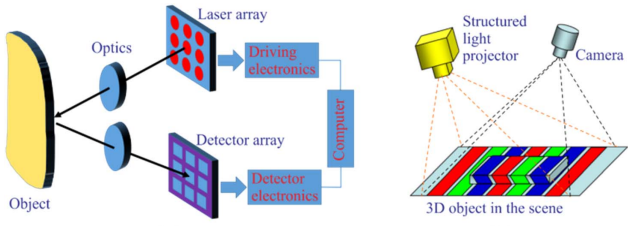

Fig. 8. (a) Schematic of focal plane scanning [148,151]. (b) Illustration of structured light [153].

2D pattern often consists of randomly distributed dots, which can be realized by the arrangement of the elements of the array.

5. VCSELs WITH HIGH-CONTRAST METASTRUCTURES

Extensive research on surface metastructures or nanostructures has been carried out in the past decade, and many applications have been suggested to use their unique optical properties. High-index-contrast 1D wavelength gratings, also called high-contrast gratings (HCGs), and the 2D variation of such structures, generalized high-contrast metastructures (HCMs), have been and continue to be the focus of intense research. Here we focus on 1D HCGs and VCSELs with 1D HCGs. 2D HCMs have been comprehensively reviewed recently elsewhere [154,155].

A. Fundamentals of HCGs

A HCG reflector, also called a photonic crystal mirror or a guided-mode resonant reflector [156–158], is shown in Fig. 9(a). The grating bars (also called stripes) composed of the high-index material in the HCG are fully immersed in a low refractive index medium, e.g., the air, resulting in a high index contrast. The grating period (Λ) is a value in units of length that is between the wavelength in the high refractive index material and the wavelength in the low refractive index material. To simplify the modeling, the numbers of bars and periods and the length of the bars may all be taken to be infinite-size. Figure 9(b) shows that the first two waveguide array modes in infinite HCGs with real propagation constants have a π-phase difference in the output plane and cancel each other, causing a nearly 100% reflection [159]. When two such 100% reflectivity points are located closely in the spectrum, a high-reflectivity broadband is obtained. There are alternative interpretations for the observed high-reflectivity broadband of HCGs based on Fano resonance or guided-mode resonance [155,158]. A broadband and high-reflectivity HCG can serve as a reflector and replace the top DBR partially or fully [160–163]. Experimentally, HCG-VCSELs show an excellent mode selectivity and polarization control, even for large oxide apertures.

For the HCG design, the structure parameters can be optimized by rigorous coupled wave analysis (RCWA) [164] and analytical methods [159]. These two methods consider that HCGs are of an infinite size and the incident wave is an infinite plane wave. The infinite-size HCG model is useful to rapidly search the parameters of HCGs. However, in real devices the reflectivity may be reduced, caused by the finite size [165] and by imperfect (nonrectangular) stripes, which increases the threshold current, causing a reduced energy efficiency of the VCSELs. The finite-size incident wave can excite guide modes in the HCG by higher-order angular components. The excited guided modes reduce the reflectivity and increase the transmission [166]. These excited guided modes can redirect the incident wave to the in-plane direction, providing the potential for an integrated optical sensor and for integration with planar optical circuits [167,168]. Therefore, it is indispensable to calculate the finite-size HCG properties by a finite difference time domain method after choosing the HCG parameters using RCWA or analytical methods.

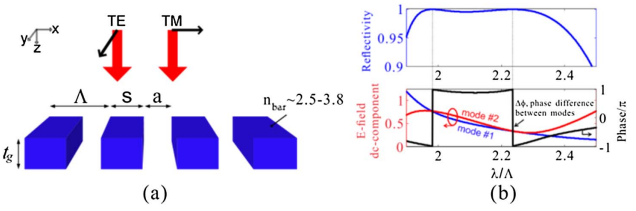

Fig. 9. (a) Schematic of an HCG. The red arrows show the direction of wave incidence. The black arrows indicate the E-field direction in both TE and TM polarizations of incidence. (b) Double-mode solution exhibiting perfect intensity cancellation at the HCG output plane leading to 100% reflectivity [159].

HCGs also show a strong ability to confine the field. The energy penetration depth of HCGs is much smaller than that of DBRs [169]. The small energy penetration depth is beneficial to construct a short cavity leading to a large confinement factor. The small mode volume is beneficial to enhance the Purcell factor, reducing the carrier lifetime to achieve a larger modulation bandwidth and energy efficiency [102,103]. In HCGs, the phase penetration depth, which partly controls the photon lifetime, can be tuned by the physical structure parameters without degrading the reflectivity, unlike the shallow surface etching method [38,170]. The increased confinement factor and the optimum photon lifetime combined with a high reflectivity are expected to increase the relaxation resonance frequency, lower the damping factor, and lower the threshold current, which are all factors that are decisive for high-speed modulation and energy-efficient operation.

In fabricating HCG-VCSELs, a sacrificial layer below the HCG layer is always removed to create a suspended HCG surrounded by a low refractive index material (for example, air). Alternatively, epitaxial AlGaAs that is selectively oxidized to form the low refractive index material AlGaO may be used as the underlying low refractive index layer. Therefore, a lattice matched material system is essential from the perspective of both device performance and fabrication feasibility. Recently zero-contrast gratings (ZCGs) have been proposed to replace completely or partly the top DBR [171–174]. The sacrificial layer removal step in the HCG fabrication is not required for the ZCG fabrication. The whole device fabrication is thus highly simplified, and the mechanical stability is improved. ZCGs also can achieve a high reflectivity beyond 99.5% due to the destructive interference at the output plane but with a narrower high reflectance bandwidth compared to HCGs, and they can show a better mode selectivity for ZCG-VCSELs. ZCGs are less complex in the overall VCSEL fabrication but they have rather tight geometrical tolerances. For a ± 10 nm variation of the etching depth of 304 nm, the wavelength of the maximum reflectivity shifts by ± 7 nm, and the reflection phase change is 0.1π for a ZCG designed for use in the 980 nm range [175].

B. VCSELs with Metastructures

The first electrical HCG-VCSEL reported in 2007 was realized at 850 nm in the GaAs material system as shown in Fig. 10(a) [160]. It used HCGs to replace part of the top DBR and kept four DBR pairs to provide current spreading and active

region protection. These devices showed a sub-milliampere threshold current and single-mode and polarization-selective operation. Later 1060 nm and 1550 nm HCG-VCSELs were realized [162,176]. The reflectivity of an HCG strongly depends on the HCG size, the HCG parameters, the incident angle, the polarization, and the sizes of the incident beam [163,166,177–179]. Thus, it is easy for an HCG-VCSEL to realize single-mode operation even with a large oxide aperture [165]. The output beam pattern can be shaped by the HCG, which was predicted in 2014 [166]. In 2018, HCG-VCSELs realized single-lobe, double-lobe, triple-lobe, "bow-tie," "sugar cone," and "doughnut" beam patterns without any external optics [177], as shown in Fig. 10(b). Figure 10(c) is the schematic of a nanoelectromechanical tunable HCG-VCSEL developed for a wide tuning range and fast tuning because of the compact HCG mirrors compared to existing DBR-based electrostatic-actuated microelectromechanical tunable VCSELs [162,180,181]. Such tunable HCG-VCSELs have been realized in the 850, 1060, and 1550 nm wavelength ranges.

HCG reflectors are resonant structures, very different from DBRs, and the reflection phase can be tuned while keeping a high reflectivity [170]. By adjusting the HCG parameters like period and duty cycle, different wavelengths of HCG-VCSELs on a single wafer can be simultaneously achieved [182]. Therefore, HCG-VCSEL arrays [as shown in Fig. 10(d)] with multiple uniformly spaced wavelengths can be constructed on a single HCG-VCSEL wafer for wavelength-division multiplexing (WDM), providing a promising way to increase the aggregate bandwidth of a single fiber. Optically pumped HCG-VCSEL arrays were reported with double silicon-based HCGs as reflectors for dense WDM at 1.55 μm [183]. A GaAs-based HCG filter array with different resonance wavelengths was demonstrated, targeting electrically pumped HCG-VCSEL arrays [184,185]. A first monolithic four-channel HCG-VCSEL array covering a wavelength span of 15 nm with 5 nm channel spacing was demonstrated at 980 nm for WDM applications [186].

Vertical coupling was also proposed to extract light from a Fabry–Perot microcavity composed of double HCG mirrors to a Si waveguide [187]. This is a feasible approach to realize the integration of a vertical cavity laser with in-plane PICs, as discussed in Section 3.E. Very recently, HCGs have been proposed to replace the DBR as reflectors and at the same time to route the emitting light into the in-plane waveguides [188,189], as shown in Figs. 11(a) and 11(b). This approach reduces the thermal resistance of the devices. Optically pumped hybrid vertical-cavity lasers with lateral emission into a silicon waveguide were reported using a silicon HCG at 1.5 μm [190]. Experimentally, a 3 dB frequency of 27 GHz was obtained for an optically pumped laser [191]. For the short wavelength range, SiN-based HCGs were proposed to serve as reflectors and extract the light into the in-plane SiN waveguide because SiN is transparent from 600 to 1100 nm, where silicon is not suitable for waveguide circuits. Figure 11(c) shows a half-VCSEL placed onto a SiN-based HCG surrounded by SiO_2, thus forming a hybrid vertical-cavity silicon-integrated laser at 850 nm. The laser emission is in-plane directly into a SiN waveguide [192]. Continuous-wave electrically pumped operation was achieved for such a hybridly integrated laser, and a single-sided waveguide-coupled optical output power of 73 μW with a side-mode suppression ratio of 29 dB was reported with an oxide aperture diameter of 5 μm in the top half-VCSEL. These integrated laser sources in densely integrated circuits have the potential for applications in medical point-of-care devices, body implants for monitoring of glucose levels, and sensing devices integrated into smartphones. Another variation of the HCG-VCSEL uses a composite monolithic high-contrast grating and DBR as the top coupling

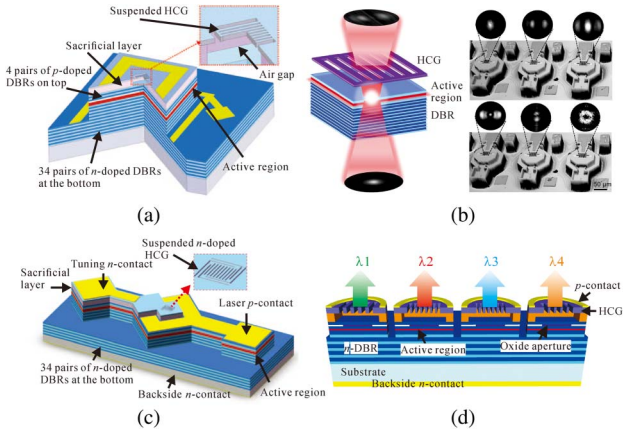

Fig. 10. (a) Schematic of an HCG-VCSEL [160]. (b) HCG-VCSEL array for single-lobe, double-lobe, triple-lobe, "bow-tie," "sugar cone," and "doughnut" beam patterns [177]. (c) Schematic of a nanoelectromechanical tunable VCSEL using the highly reflective HCG as its top mirror, instead of conventional DBRs [180]. (d) Schematic of a monolithic HCG-VCSEL array with different HCG parameters.

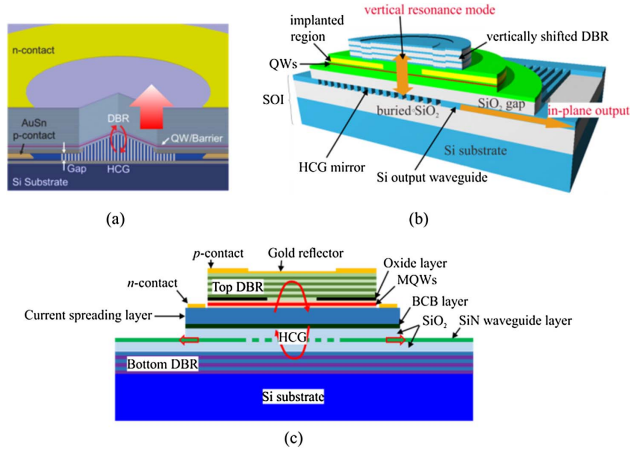

Fig. 11. (a) Schematic of a VCSEL with a silicon HCG as a bottom mirror. An HCG serves as the bottom mirror and potentially serves as a waveguide coupler for an in-plane SOI waveguide, facilitating the integration of a VCSEL with in-plane silicon photonic circuits [188]. (b) Schematic of a vertical-cavity laser with lateral emission into a silicon waveguide via an HCG [189]. (c) Schematic of a vertical-cavity laser with in-plane out-coupling into a SiN waveguide. A subwavelength grating is inserted under a half-VCSEL to redirect the vertical resonance light to the in-plane SiN waveguide [192].

mirror to relieve the fabrication complexity. The first electrically injected VCSEL that includes this type of a monolithic HCG was reported in 2018 [193].

6. CONCLUSIONS AND PROSPECTS

VCSELs have unique advantages compared to edge-emitting lasers. Impressive progress has been achieved enabling energy-efficient and fast data communication in the past decade. Novel device designs based on the deeply developed insights to the device physics and to advanced modulation formats have been used to boost the performance of VCSELs. Data rates beyond 50 Gbps in the on–off keying modulation format have been demonstrated. An energy efficiency of close to 50 fJ/bit was reported at 25°C for a small oxide aperture VCSEL. An error-free transmission rate of 50 Gbps at 90°C was also demonstrated. To increase the capacity of MMF-based links, the PAM4 modulation format is employed, yielding a 100 Gbps data rate in a single lane. 400 Gbps via SWDM was also achieved.

VCSELs will continue to be the dominant laser sources in data centers and HPCs and might penetrate chip-to-chip and even on-chip optical interconnects. Single-mode VCSELs with a reduced spectral width will attract significant interest for extended distance transmission over MMF for data centers and HPCs [66,86,87,194–198]. Advanced modulation formats like carrierless amplitude phase (CAP) or discrete multi-tone (DMT) for high-speed VCSEL transmission are promising to increase the transmission data rates beyond 100 Gbps with a high spectral efficiency [199,200]. Low-loss and straightforward coupling between VCSELs and in-plane PICs is still challenging. The integration of VCSELs with PICs via metastructures makes the chips compact and power efficient. Such VCSEL-based integrated chips have important applications in optical interconnects, optical sensors, and consumer electronics. VCSELs with metastructures can provide different orbital angular modes [201] and laser modes [177], opening a new way for increasing the capacity of links.

VCSELs have unique advantages over silicon photonics technology, which is presently a hot topic [84]. VCSELs have a lower cost, lower power consumption (1.8 pJ/bit), and a smaller footprint (~8 μm emitting area in diameter) enabling a large bandwidth density, while a silicon photonic transmitter consisting of one continuous-wave semiconductor laser and a Mach–Zehnder modulator requires about 10 pJ/bit at 25 Gbps and takes up a footprint of about 300 μm. VCSELs will continue to be the lowest cost and highest energy efficiency light source for data links available for short-reach optical interconnects.

VCSEL-based sensors have wide applications in consumer electronics, car markets, Internet of Things, atomic sensing [202], and much more. VCSELs featuring low energy consumption, small footprint, and an array configuration will undoubtedly be the dominant laser sources for these and many other applications. As VCSELs will become essential for various sensor applications in our daily life, they will receive increasing attention from industry and academic communities.

Funding. National Natural Science Foundation of China (NSFC) (61675193); Pioneer Hundred Talents Program, Chinese Academy of Sciences (CAS); Collaborative Research Center (Sonderforschungsbereich - SFB) 787, Deutsche Forschungsgemeinschaft (DFG); Distinguished Fellowship of the President of the Chinese Academy of Sciences.

REFERENCES

1. I. Melngailis, "Longitudinal injection plasma laser of InSb," Appl. Phys. Lett. **6**, 59–60 (1965).
2. H. Soda, K. Iga, C. Kitahara, and Y. Suematsu, "GaInAsP/InP surface emitting injection lasers," Jpn. J. Appl. Phys. **18**, 2329–2330 (1979).
3. J. P. van der Ziel and M. Ilegems, "Multilayer GaAs-$A1_{0.3}Ga_{0.7}As$ dielectric quarter wave stacks grown by molecular beam epitaxy," Appl. Opt. **14**, 2627–2630 (1975).
4. M. Ogura, T. Hata, N. J. Kawai, and T. Yao, "GaAs/$Al_xGa_{1-x}As$ multilayer reflector for surface emitting laser diode," Jpn. J. Appl. Phys. **22**, L112–L114 (1983).
5. M. Ogura, T. Hata, and T. Yao, "Distributed feedback surface emitting laser diode with multilayered heterostructure," Jpn. J. Appl. Phys. **23**, L512–L514 (1984).
6. M. Ogura and T. Yao, "Surface emitting laser diode with $Al_xGa_{1-x}As$/GaAs multilayered heterostructure," J. Vac. Sci. Technol. B **3**, 784–787 (1985).
7. K. Iga, S. Kinoshita, and F. Koyama, "Microcavity GaAlAs/GaAs surface-emitting laser with I_{th} = 6 mA," Electron. Lett. **23**, 134–136 (1987).
8. T. Sakaguchi, F. Koyama, and K. Iga, "Vertical cavity surface-emitting laser with an AlGaAs/AlAs Bragg reflector," Electron. Lett. **24**, 928–929 (1988).
9. P. L. Gourley and T. J. Drummond, "Visible, room temperature, surface emitting laser using an epitaxial Fabry–Perot resonator with AlGaAs/AlAs quarter-wave high reflectors and AlGaAs/GaAs multiple quantum wells," Appl. Phys. Lett. **50**, 1225–1227 (1987).
10. J. L. Jewell, A. Scherer, S. L. McCall, Y. H. Lee, S. Walker, J. P. Harbison, and L. T. Florez, "Low-threshold electrically pumped vertical-cavity surface-emitting microlasers," Electron. Lett. **25**, 1123–1134 (1989).
11. Y. H. Lee, J. L. Jewell, A. Scherer, S. L. McCall, J. P. Harbison, and L. T. Florez, "Room-temperature continuous-wave vertical-cavity single-quantum-well microlaser diodes," Electron. Lett. **25**, 1377–1378 (1989).
12. Y. H. Lee, B. Tell, K. Brown-Goebeler, J. L. Jewell, and J. V. Hove, "Top-surface-emitting GaAs four-quantum-well lasers emitting at 0.85 μm," Electron. Lett. **26**, 710–711 (1990).
13. R. S. Geels, S. W. Corzine, J. W. Scott, D. B. Young, and L. A. Coldren, "Low threshold planarized vertical-cavity surface-emitting lasers," IEEE Photon. Technol. Lett. **2**, 234–236 (1990).
14. J. M. Dallesasse, N. Holonyak, Jr., A. R. Sugg, T. A. Richard, and N. El-Zein, "Hydrolyzation oxidation of $Al_xGa_{1-x}As$-AlAs-GaAs quantum well heterostructures and superlattices," Appl. Phys. Lett. **57**, 2844–2846 (1990).
15. D. L. Huffaker, D. G. Deppe, K. Kumar, and T. J. Rogers, "Native-oxide defined ring contact for low threshold vertical-cavity lasers," Appl. Phys. Lett. **65**, 97–99 (1994).
16. K. D. Choquette, K. M. Geib, C. I. H. Ashby, R. D. Twesten, O. Blum, H. Q. Hou, D. M. Follstaedt, B. E. Hammons, D. Mathes, and R. Hull, "Advances in selective wet oxidation of AlGaAs alloys," IEEE J. Sel. Top. Quantum Electron. **3**, 916–926 (1997).
17. M. Dallesasse and N. Holonyak, Jr., "Oxidation of Al-bearing III-V materials: a review of key progress," J. Appl. Phys. **113**, 051101 (2013).
18. F. Koyama, "Recent advances of VCSEL photonics," J. Lightwave Technol. **24**, 4502–4513 (2006).
19. H. Li, P. Wolf, P. Moser, G. Larisch, J. A. Lott, and D. Bimberg, "Vertical-cavity surface-emitting lasers for optical interconnects," SPIE Newsroom (2014), DOI: 10.1117/2.1201411.005689.
20. A. Larsson, "Advances in VCSELs for communication and sensing," IEEE J. Sel. Top. Quantum Electron. **17**, 1552–1567 (2011).

21. R. Michalzik, *VCSELs - Fundamentals, Technology and Applications of Vertical-Cavity Surface-Emitting Lasers*, Springer Series in Optical Sciences (Springer, 2013), Vol. **166**.
22. J. A. Tatum, "VCSEL proliferation," Proc. SPIE **6484**, 648403 (2014).
23. M. Grabherr, "New applications boost VCSEL quantities: recent developments at Philips," Proc. SPIE **9381**, 938102 (2015).
24. C. Wilmsen, H. Temkin, and L. A. Coldren, eds., *Vertical Cavity Surface Emitting Lasers: Design, Fabrication, Characterization and Applications* (Cambridge University, 1999).
25. H. E. Li and K. Iga, *Vertical-Cavity Surface-Emitting Laser Devices*, Springer Series in Photonics (Springer, 2003), Vol. **6**.
26. J.-F. Seurin, D. Zhou, G. Xu, A. Miglo, D. Li, T. Chen, B. Guo, and C. Ghosh, "High-efficiency VCSEL arrays for illumination and sensing in consumer applications," Proc. SPIE **9766**, 97660D (2016).
27. N. Mukoyama, H. Otoma, J. Sakurai, N. Ueki, and H. Nakayama, "VCSEL array-based light exposure system for laser printing," Proc. SPIE **6908**, 69080H (2008).
28. D. Zhou, J.-F. Seurin, G. Xu, R. V. Leeuwen, A. Miglo, Q. Wang, A. Kovsh, and C. Ghosh, "Progress on high-power 808 nm VCSELs and applications," Proc. SPIE **10122**, 1012206 (2007).
29. H. Moench, R. Conrads, S. Gronenborn, X. Gu, M. Miller, P. Pekarski, J. Pollman-Retsch, A. Pruijmboom, and U. Weichmann, "Integrated high power VCSEL systems," Proc. SPIE **9733**, 97330V (2016).
30. M. Müller, W. Hofmann, T. Gründl, M. Horn, P. Wolf, R. D. Nagel, E. Rönneberg, G. Böhm, D. Bimberg, and M.-C. Amann, "1550-nm high-speed short-cavity VCSELs," IEEE J. Sel. Top. Quantum Electron. **17**, 1158–1166 (2011).
31. S. Spiga, W. Soenen, A. Andrejew, D. M. Schoke, X. Yin, J. Bauwelinck, G. Boehm, and M.-C. Amann, "Single-mode high-speed 1.5-μm VCSELs," J. Lightwave Technol. **35**, 727–733 (2017).
32. A. Caliman, A. Mereuta, P. Wolf, A. Sirbu, V. Iakovlev, D. Bimberg, and E. Kapon, "25 Gbps direct modulation and 10 km data transmission with 1310 nm waveband wafer fused VCSELs," Opt. Express **24**, 16329–16335 (2016).
33. T.-C. Lu, C.-C. Kao, H.-C. Kuo, G.-S. Huang, and S.-C. Wang, "CW lasing of current injection blue GaN-based vertical cavity surface emitting laser," Appl. Phys. Lett. **92**, 141102 (2008).
34. L. A. Coldren, S. W. Corzine, and M. L. Mašanović, *Diode Lasers and Photonic Integrated Circuits*, 2nd ed. (Wiley, 2012).
35. I. Suemune, "Theoretical study of differential gain in strained quantum well structures," IEEE J. Quantum Electron. **27**, 1149–1159 (1991).
36. P. Westbergh, J. S. Gustavsson, Å. Haglund, M. Sköld, A. Joel, and A. Larsson, "High-speed, low-current-density 850 nm VCSELs," IEEE J. Sel. Top. Quantum Electron. **15**, 694–703 (2009).
37. S. B. Healy, E. P. O'Reilly, J. S. Gustavsson, P. Westbergh, Å. Haglund, A. Larsson, and A. Joel, "Active region design for high-speed 850-nm VCSELs," IEEE J. Quantum Electron. **46**, 506–512 (2010).
38. P. Westbergh, J. S. Gustavsson, B. Kögel, Å. Haglund, and A. Larsson, "Impact of photon lifetime on high-speed VCSEL performance," IEEE J. Sel. Top. Quantum Electron. **17**, 1603–1613 (2011).
39. G. Larisch, P. Moser, J. A. Lott, and D. Bimberg, "Impact of photon lifetime on the temperature stability of 50 Gb/s 980 nm VCSELs," IEEE Photon. Technol. Lett. **28**, 2327–2330 (2016).
40. W. Hofmann, P. Moser, P. Wolf, A. Mutig, M. Kroh, and D. Bimberg, "44 Gb/s VCSEL for optical interconnects," in *Optical Fiber Communication Conference* (2011), paper PDPC5.
41. P. Moser, P. Wolf, A. Mutig, G. Larisch, W. Unrau, W. Hofmann, and D. Bimberg, "85°C error-free operation at 38 Gb/s of oxide-confined 980-nm vertical-cavity surface-emitting lasers," Appl. Phys. Lett. **100**, 081103 (2012).
42. H. W. Then, C. H. Wu, M. Feng, and N. Holonyak, Jr., "Microwave characterization of Purcell enhancement in a microcavity laser," Appl. Phys. Lett. **96**, 131107 (2010).
43. P. Zhou, J. Cheng, C. F. Schaus, S. Z. Sun, K. Zheng, E. Armour, C. Hains, W. Hsin, D. R. Myers, and G. A. Vawter, "Low series resistance high-efficiency GaAs/AlGaAs vertical-cavity surface-emitting lasers with continuously graded mirrors grown by MOCVD," IEEE Photon. Technol. Lett. **3**, 591–593 (1991).
44. M. A. Afromowitz, "Thermal conductivity of $Ga_{1-x}Al_xAs$ alloys," J. Appl. Phys. **44**, 1292–1294 (1973).
45. K. Lascola, W. Yuen, and C. Chang-Hasnain, "Structural dependence of the thermal resistance of vertical cavity surface emitting lasers," in *IEEE/LEOS Summer Topical Meeting* (1997), pp. 79–80.
46. A. N. AL-Omari, M. S. Alias, A. Ababneh, and K. L. Lear, "Improved performance of top-emitting oxide-confined polyimide-planarized 980 nm VCSELs with copper-plated heat sinks," J. Phys. D **45**, 505101 (2012).
47. R. Pu, C. W. Wilmsen, K. M. Geib, and K. D. Choquette, "Thermal resistance of VCSEL's bonded to integrated circuits," IEEE Photon. Technol. Lett. **11**, 1554–1556 (1999).
48. E. F. Schubert, L. W. Tu, G. J. Zydzik, R. F. Kopf, A. Benvenuti, and M. R. Pinto, "Elimination of heterojunction band discontinuities by modulation doping," Appl. Phys. Lett. **60**, 466–468 (1992).
49. A. N. AL-Omari and K. L. Lear, "Polyimide-planarized vertical-cavity surface-emitting lasers with 17.0-GHz bandwidth," IEEE Photon. Technol. Lett. **16**, 969–971 (2004).
50. Y.-C. Chang, C. S. Wang, and L. A. Coldren, "High-efficiency, high-speed VCSELs with 35 Gbit/s error-free operation," Electron. Lett. **43**, 1022–1023 (2007).
51. M. Azuchi, N. Jikutani, M. Ami, T. Kondo, and F. Koyama, "Multioxide layer vertical-cavity surface-emitting lasers with improved modulation bandwidth," in *5th Pacific Rim Conference on Lasers and Electro-Optics* (2003), Vol. **1**, p. 163.
52. Y.-C. Chang, C. S. Wang, L. A. Johansson, and L. A. Coldren, "High-efficiency, high-speed VCSELs with deep oxidation layers," Electron. Lett. **42**, 1281–1282 (2006).
53. N. Suzuki, H. Hatakeyama, K. Fukatsu, T. Anan, K. Yashiki, and M. Tsuji, "25 Gbit/s operation of InGaAs-based VCSELs," Electron. Lett. **42**, 975–976 (2006).
54. D. M. Kuchta, P. Pepeljugoski, and Y. Kwark, "VCSEL modulation at 20 Gb/s over 200 m of multimode fiber using a 3.3 V SiGe laser driver IC," in *Digest of LEOS Summer Topical Meetings: Advanced Semiconductor Lasers and Applications/Ultraviolet and Blue Lasers and Their Applications/Ultralong Haul DWDM Transmission and Networking/WDM Compo* (2001), pp. 49–50.
55. R. H. Johnson and D. M. Kuchta, "30 Gb/s directly modulated 850 nm datacom VCSELs," in *Conference on Lasers and Electro-Optics* (2008), paper CPDB2.
56. P. Westbergh, J. S. Gustavsson, Å. Haglund, A. Larsson, F. Hopfer, G. Fiol, D. Bimberg, and A. Joel, "32 Gbit/s multimode fibre transmission using high-speed, low current density 850 nm VCSEL," Electron. Lett. **45**, 366–368 (2009).
57. P. Westbergh, J. S. Gustavsson, B. Kögel, Å. Haglund, A. Larsson, A. Mutig, A. Nadtochiy, D. Bimberg, and A. Joel, "40 Gbit/s error-free operation of oxide-confined 850 nm VCSEL," Electron. Lett. **46**, 1014–1016 (2010).
58. P. Westbergh, R. Safaisini, E. Haglund, B. Kögel, J. S. Gustavsson, A. Larsson, M. Geen, R. Lawrence, and A. Joel, "High-speed 850 nm VCSELs with 28 GHz modulation bandwidth operating error-free up to 44 Gbit/s," Electron. Lett. **48**, 1145–1147 (2012).
59. P. Westbergh, E. P. Haglund, E. Haglund, R. Safaisini, J. S. Gustavsson, and A. Larsson, "High-speed 850 nm VCSELs operating error free up to 57 Gbit/s," Electron. Lett. **49**, 1021–1023 (2013).
60. E. Haglund, P. Westbergh, J. S. Gustavsson, E. P. Haglund, A. Larsson, M. Geen, and A. Joel, "30 GHz bandwidth 850 nm VCSEL with sub-100 fJ/bit energy dissipation at 25-50 Gbit/s," Electron. Lett. **51**, 1096–1098 (2015).
61. A. Mutig, S. A. Blokhin, A. M. Nadtochiy, G. Fiol, J. A. Lott, V. A. Shchukin, N. N. Ledentsov, and D. Bimberg, "Frequency response of large aperture oxide-confined 850 nm vertical cavity surface emitting lasers," Appl. Phys. Lett. **95**, 131101 (2009).
62. S. A. Blokhin, J. A. Lott, A. Mutig, G. Fiol, N. N. Ledentsov, M. V. Maximov, A. M. Nadtochiy, V. A. Shchukin, and D. Bimberg, "Oxide-confined 850 nm VCSELs operating at bit rates up to 40 Gbit/s," Electron. Lett. **45**, 501–502 (2009).

63. F. Tan, M.-K. Wu, M. Liu, M. Feng, and N. Holonyak, Jr., "850 nm oxide-VCSEL with low relative intensity noise and 40 Gb/s error free data transmission," IEEE Photon. Technol. Lett. **26**, 289–292 (2014).
64. M. Liu, C. Y. Wang, M. Feng, and N. Holonyak, Jr., "850 nm oxide-confined VCSELs with 50 Gb/s error-free transmission operating up to 85°C," in *Conference on Lasers and Electro-Optics* (2016), paper SF1L.6.
65. J.-W. Shi, J.-C. Yan, J.-M. Wun, J. Chen, and Y.-J. Yang, "Oxide-relief and Zn-diffusion 850-nm vertical-cavity surface-emitting lasers with extremely low energy-to-data-rate ratios for 40 Gbit/s operations," IEEE J. Sel. Top. Quantum Electron. **19**, 7900208 (2013).
66. K.-L. Chi, J.-L. Yen, J.-M. Wun, J.-W. Jiang, I.-C. Lu, J. Chen, Y.-J. Yang, and J.-W. Shi, "Strong wavelength detuning of 850 nm vertical-cavity surface-emitting lasers for high-speed (>40 Gbit/s) and low-energy consumption operation," IEEE J. Sel. Top. Quantum Electron. **21**, 1701510 (2015).
67. Y.-C. Chang and L. A. Coldren, "Efficient, high-data-rate, tapered oxide-aperture vertical-cavity surface-emitting lasers," IEEE J. Sel. Top. Quantum Electron. **15**, 704–715 (2009).
68. P. Moser, J. A. Lott, P. Wolf, G. Larisch, H. Li, and D. Bimberg, "Error-free 46 Gbit/s operation of oxide-confined 980 nm VCSELs at 85°C," Electron. Lett. **50**, 1369–1371 (2014).
69. N. Haghighi, G. Larisch, R. Rosales, M. Zorn, and J. A. Lott, "35 GHz bandwidth with directly current modulated 980 nm oxide aperture single cavity VCSELs," in *IEEE International Semiconductor Laser Conference (ISLC)* (2018), paper WD4.
70. E. Simpanen, J. S. Gustavsson, E. Haglund, E. P. Haglund, A. Larsson, W. V. Sorin, S. Mathai, and M. R. Tan, "1060 nm single-mode vertical-cavity surface-emitting laser operating at 50 Gbit/s data rate," Electron. Lett. **53**, 869–871 (2017).
71. K. Yashiki, N. Suzuki, K. Fukatsu, T. Anan, H. Hatakeyama, and M. Tsuji, "1.1-μm-range high-speed tunnel junction vertical-cavity surface-emitting lasers," IEEE Photon. Technol. Lett. **19**, 1883–1885 (2007).
72. T. Anan, N. Suzuki, K. Yashiki, K. Fukatsu, H. Hatakeyama, T. Akagawa, K. Tokutome, and M. Tsuji, "High-speed 1.1-μm-range InGaAs VCSELs," in *Optical Fiber Communication Conference* (2008), paper OthS5.
73. D. M. Kuchta, A. V. Rylyakov, F. E. Doany, C. L. Schow, J. E. Proesel, C. W. Baks, P. Westbergh, J. S. Gustavsson, and A. Larsson, "A 71-Gb/s NRZ modulated 850-nm VCSEL-based optical link," IEEE Photon. Technol. Lett. **27**, 577–580 (2015).
74. E. Haglund, P. Westbergh, J. S. Gustavsson, E. P. Haglund, and A. Larsson, "High-speed VCSELs with strong confinement of optical fields and carriers," J. Lightwave Technol. **34**, 269–277 (2015).
75. D. M. Kuchta, A. V. Rylyakov, C. L. Schow, J. E. Proesel, C. Baks, C. Kocot, L. Graham, R. Johnson, G. Landry, E. Shaw, A. MacInnes, and J. Tatum, "A 55 Gb/s directly modulated 850 nm VCSEL-based optical link," in *IEEE Photonics Conference* (2012), paper PD1.5.
76. D. M. Kuchta, C. L. Schow, A. V. Rylyakov, J. E. Proesel, F. E. Doany, C. Baks, B. H. Hamel-Bissell, C. Kocot, L. Graham, R. Johnson, G. Landry, E. Shaw, A. MacInnes, and J. Tatum, "A 56.1 Gb/s NRZ modulated 850 nm VCSEL-based optical link," in *Optical Fiber Communication Conference* (2013), paper OW1B.5.
77. M. Liu, C. Y. Wang, M. Feng, and N. Holonyak, Jr., "50 Gb/s error-free data transmission of 850 nm oxide-confined VCSELs," in *Optical Fiber Communication Conference* (2016), paper Tu3D.2.
78. H. Nasu, "Short-reach optical interconnects employing high-density parallel-optical modules," IEEE J. Sel. Top. Quantum Electron. **16**, 1337–1346 (2010).
79. P. Wolf, P. Moser, G. Larisch, W. Hofmann, and D. Bimberg, "High-speed and temperature-stable, oxide-confined 980-nm VCSELs for optical interconnects," IEEE J. Sel. Top. Quantum Electron. **19**, 1701207 (2013).
80. P. Moser, J. A. Lott, G. Larisch, and D. Bimberg, "Impact of the oxide-aperture diameter on the energy efficiency, bandwidth, and temperature stability of 980-nm VCSELs," J. Lightwave Technol. **33**, 825–831 (2015).
81. R. Rosales, M. Zorn, and J. A. Lott, "30-GHz bandwidth with directly current-modulated 980-nm oxide-aperture VCSELs," IEEE Photon. Technol. Lett. **29**, 2107–2110 (2017).
82. N. Haghighi, R. Rosales, G. Larisch, M. Gębski, L. Frasunkiewicz, T. Czyszanowski, and J. A. Lott, "Simplicity VCSELs," Proc. SPIE **10552**, 105520N (2018).
83. N. Suzuki, H. Hatakeyama, K. Fukatsu, T. Anan, K. Yashiki, and M. Tsuji, "25-Gbps operation of 1.1-μm-range InGaAs VCSELs for high-speed optical interconnections," in *Optical Fiber Communication Conference* (2006), paper OFA4.
84. D. Mahgerefteh, C. Thompson, C. Cole, G. Denoyer, T. Nguyen, I. Lyubomirsky, C. Kocot, and J. Tatum, "Techno-economic comparison of silicon photonics and multimode VCSELs," J. Lightwave Technol. **34**, 233–242 (2016).
85. H. Liu, C. F. Lam, and C. Johnson, "Scaling optical interconnects in datacenter networks opportunities and challenges for WDM," in *IEEE Symposium on High Performance Interconnects* (2010), pp. 113–116.
86. P. Moser, J. A. Lott, P. Wolf, G. Larisch, H. Li, and D. Bimberg, "85-fJ dissipated energy per bit at 30 Gb/s across 500-m multimode fiber using 850-nm VCSELs," IEEE Photon. Technol. Lett. **25**, 1638–1641 (2013).
87. R. Safaisini, E. Haglund, P. Westbergh, J. S. Gustavsson, and A. Larsson, "20 Gbit/s data transmission over 2 km multimode fibre using 850 nm mode filter VCSEL," Electron. Lett. **50**, 40–42 (2014).
88. H. Dalir and F. Koyama, "29 GHz directly modulated 980 nm vertical-cavity surface emitting lasers with bow-tie shape transverse coupled cavity," Appl. Phys. Lett. **103**, 091109 (2013).
89. S. T. M. Fryslie, M. P. Tan, D. F. Siriani, M. T. Johnson, and K. D. Choquette, "37-GHz modulation via resonance tuning in single-mode coherent vertical-cavity laser arrays," IEEE Photon. Technol. Lett. **27**, 415–418 (2015).
90. B. Tell, K. F. Brown-Goebeler, R. E. Leibenguth, F. M. Baez, and Y. H. Lee, "Temperature dependence of GaAs-AlGaAs vertical cavity surface emitting lasers," Appl. Phys. Lett. **60**, 683–685 (1992).
91. L. A. Graham, H. Chen, D. Gazula, T. Gray, J. K. Guenter, B. Hawkins, R. Johnson, C. Kocot, A. N. MacInnes, G. D. Landry, and J. A. Tatum, "The next generation of high speed VCSELs at Finisar," Proc. SPIE **8276**, 827602 (2012).
92. C. Xie, N. Li, S. Huang, C. Liu, L. Wang, and K. P. Jackson, "The next generation high data rate VCSEL development at SEDU," Proc. SPIE **8639**, 863903 (2013).
93. P. Westbergh, R. Safaisini, E. Haglund, J. S. Gustavsson, A. Larsson, M. Geen, R. Lawrence, and A. Joel, "High-speed oxide confined 850-nm VCSELs operating error-free at 40 Gb/s up to 85°C," IEEE Photon. Technol. Lett. **25**, 768–771 (2013).
94. D. M. Kuchta, A. V. Rylyakov, C. L. Schow, J. E. Proesel, C. W. Baks, P. Westbergh, J. S. Gustavsson, and A. Larsson, "A 50 Gb/s NRZ modulated 850 nm VCSEL transmitter operating error free to 90°C," J. Lightwave Technol. **33**, 802–810 (2015).
95. N. Ledentsov, Jr., M. Agustin, J.-R. Kropp, V. A. Shchukin, V. P. Kalosha, K. L. Chi, Z. Khan, J. W. Shi, and N. N. Ledentsov, "Temperature stable oxide-confined 850 nm VCSELs operating at bit rates up to 25 Gbit/s at 150°C," Proc. SPIE **10552**, 105520P (2018).
96. P. Moser, W. Hofmann, P. Wolf, J. A. Lott, G. Larisch, A. Payusov, N. N. Ledentsov, and D. Bimberg, "81 fJ/bit energy-to-data ratio of 850 nm vertical-cavity surface-emitting lasers for optical interconnects," Appl. Phys. Lett. **98**, 231106 (2011).
97. A. Mutig, G. Fiol, P. Moser, D. Arsenijevic, V. A. Shchukin, N. N. Ledentsov, S. S. Mikhrin, I. L. Krestnikov, D. A. Livshits, A. R. Kovsh, F. Hopfer, and D. Bimberg, "120°C 20 Gbit/s operation of 980 nm VCSEL," Electron. Lett. **44**, 1305–1306 (2008).
98. H. Li, P. Wolf, P. Moser, G. Larisch, A. Mutig, J. A. Lott, and D. Bimberg, "Energy-efficient and temperature-stable oxide-confined 980 nm VCSELs operating error-free at 38 Gbit/s at 85°C," Electron. Lett. **50**, 103–105 (2014).
99. H. Li, P. Wolf, P. Moser, G. Larisch, J. A. Lott, and D. Bimberg, "Temperature-stable 980-nm VCSELs for 35-Gb/s operation at 85°C with 139-fJ/bit dissipated heat," IEEE Photon. Technol. Lett. **26**, 2349–2352 (2014).
100. D. A. B. Miller, "Device requirements for optical interconnects to silicon chips," Proc. IEEE **97**, 1166–1185 (2009).

101. P. Moser, J. A. Lott, P. Wolf, G. Larisch, H. Li, N. N. Ledentsov, and D. Bimberg, "56 fJ dissipated energy per bit of oxide-confined 850 nm VCSELs operating at 25 Gbit/s," Electron. Lett. **48**, 1292–1294 (2012).
102. F. Tan, C. H. Wu, M. Feng, and N. Holonyak, Jr., "Energy efficient microcavity lasers with 20 and 40 Gb/s data transmission," Appl. Phys. Lett. **98**, 191107 (2011).
103. C. H. Wu, F. Tan, M. Feng, and N. Holonyak, Jr., "The effect of mode spacing on the speed of quantum-well microcavity lasers," Appl. Phys. Lett. **97**, 091103 (2010).
104. P. Wolf, P. Moser, G. Larisch, H. Li, J. A. Lott, and D. Bimberg, "Energy efficient 40 Gbit/s transmission with 850 nm VCSELs at 108 fJ/bit dissipated heat," Electron. Lett. **49**, 666–667 (2013).
105. J.-W. Shi, W.-C. Weng, F.-M. Kuo, J.-I. Chyi, S. Pinches, M. Geen, and A. Joel, "Oxide-relief vertical-cavity surface-emitting lasers with extremely high data-rate/power-dissipation ratios," in *Optical Fiber Communication Conference* (2011), paper OthG2.
106. H. Li, P. Wolf, P. Moser, G. Larisch, J. A. Lott, and D. Bimberg, "Temperature-stable, energy-efficient, and high-bit rate oxide-confined 980-nm VCSELs for optical interconnects," IEEE J. Sel. Top. Quantum Electron. **21**, 1700409 (2015).
107. S. Imai, K. Takaki, S. Kamiya, H. Shimizu, J. Yoshida, Y. Kawakita, T. Takagi, K. Hiraiwa, H. Shimizu, T. Suzuki, N. Iwai, T. Ishikawa, N. Tsukiji, and A. Kasukawa, "Recorded low power dissipation in highly reliable 1060-nm VCSELs for 'Green' optical interconnection," IEEE J. Sel. Top. Quantum Electron. **17**, 1614–1620 (2011).
108. T. Suzuki, M. Funabashi, H. Shimizu, K. Nagashima, S. Kamiya, and A. Kasukawa, "1060 nm 28-Gbps VCSEL developed at Furukawa," Proc. SPIE **9001**, 900104 (2014).
109. J. Lavrencik, S. Varughese, V. A. Thomas, G. Landry, Y. Sun, R. Shubochkin, K. Balemarthy, J. Tatum, and S. E. Ralph, "100 Gbps PAM-4 transmission over 100 m OM4 and wideband fiber using 850 nm VCSELs," in *European Conference and Exhibition on Optical Communication (ECOC)* (2016), paper Th.1.C5.
110. J. Lavrencik, S. Varughese, V. A. Thomas, G. Landry, Y. Sun, R. Shubochkin, K. Balemarthy, J. Tatum, and S. E. Ralph, "4λ × 100 Gbps VCSEL PAM-4 transmission over 105 m of wide band multimode fiber," in *Optical Fiber Communication Conference* (2017), paper Tu2B.6.
111. P. Wolf, H. Li, A. Caliman, A. Mereuta, V. Iakovlev, A. Sirbu, E. Kapon, and D. Bimberg, "Spectral efficiency and energy efficiency of pulse-amplitude modulation using 1.3 μm wafer-fusion VCSELs for optical interconnects," ACS Photon. **4**, 2018–2024 (2017).
112. K. Szczerba, T. Lengyel, M. Karlsson, P. A. Andrekson, and A. Larsson, "94-Gb/s 4-PAM using an 850-nm VCSEL, pre-emphasis, and receiver equalization," IEEE Photon. Technol. Lett. **28**, 2519–2521 (2016).
113. S. M. R. Motaghiannezam, I. Lyubomirsky, H. Daghighian, C. Kocot, T. Gray, J. Tatum, A. Amezcua-Correa, M. Bigot-Astruc, D. Molin, F. Achten, and P. Sillard, "180 Gbps PAM4 VCSEL transmission over 300 m wideband OM4 fibre," in *Optical Fiber Communication Conference* (2016), paper Th3G.2.
114. P. Kolesar, IEEE 802.3 50G & NGOATH Study Groups, "Wideband MMF standardization and S-WDM technology," 2016, http://www.ieee802.org/3/50G/public/Jan16/kolesar_50GE_NGOATH_01a_0116.pdf.
115. T. Aalto, M. Harjanne, M. Karppinen, M. Cherchi, A. Sitomaniemi, J. Ollila, A. Malacarne, and C. Neumeyr, "Optical interconnects based on VCSELs and low-loss silicon photonics," Proc. SPIE **10538**, 1053816 (2018).
116. P.-K. Shen, C.-T. Chen, C.-H. Chang, C.-Y. Chiu, C.-C. Chang, H.-C. Lan, Y.-C. Lee, and M.-L. Wu, "On-chip optical interconnects integrated with laser and photodetector using three-dimensional silicon waveguides," in *Optical Fiber Communication Conference* (2014), paper M2K.6.
117. Y. W. Xu, A. Michael, and C. Y. Kwok, "Fabrication of smooth 45° micromirror using TMAH low concentration solution with NCW-601A surfactant on <100> silicon," Proc. SPIE **6800**, 68001W (2008).
118. R. Santos, D. D'Agostino, F. M. Soares, H. Rabbani Haghighi, M. K. Smit, and X. J. M. Leijtens, "Fabrication and characterization of a wet-etched InP-based vertical coupling mirror," in *18th Annual Symposium of the IEEE Photonics Benelux* (2013), pp. 179–182.
119. Z. Zhang, N. Mettbach, C. Zawadzki, J. Wang, D. Schmidt, W. Brinker, N. Grote, M. Schell, and N. Keil, "Polymer-based photonic toolbox: passive components, hybrid integration and polarisation control," IET Optoelectron. **5**, 226–232 (2011).
120. D. A. Louderback, G. W. Pickrell, H. C. Lin, M. A. Fish, J. J. Hindi, and P. S. Guilfoyle, "VCSELs with monolithic coupling to internal horizontal waveguides using integrated diffraction gratings," Electron. Lett. **40**, 1064–1065 (2004).
121. J. Witzens, A. Scherer, G. Pickrell, D. Louderback, and P. Guilfoyle, "Monolithic integration of vertical-cavity surface-emitting lasers with in-plane waveguides," Appl. Phys. Lett. **86**, 101105 (2005).
122. K. S. Kaur, A. Z. Subramanian, P. Cardile, R. Verplancke, J. Van Kerrebrouck, S. Spiga, R. Meyer, J. Bauwelinck, R. Baets, and G. Van Steenberge, "Flip-chip assembly of VCSELs to silicon grating couplers via laser fabricated SU8 prisms," Opt. Express **23**, 28264–28270 (2015).
123. H. Lu, J. S. Lee, Y. Zhao, C. Scarcella, P. Cardile, A. Daly, M. Ortsiefer, L. Carroll, and P. O'Brien, "Flip-chip integration of tilted VCSELs onto a silicon photonic integrated circuit," Opt. Express **24**, 16258–16266 (2016).
124. H. Li, X. Ma, D. Yuan, Z. Zhang, E. Li, and C. Tang, "Heterogeneous integration of a III-V VCSEL light source for optical fiber sensing," Opt. Lett. **41**, 4158–4161 (2016).
125. Y. Yang, G. Djogo, M. Haque, P. R. Herman, and J. K. S. Poon, "Integration of an O-band VCSEL on silicon photonics with polarization maintenance and waveguide coupling," Opt. Express **25**, 5758–5771 (2017).
126. N. Lindenmann, G. Balthasar, D. Hillerkuss, R. Schmogrow, M. Jordan, J. Leuthold, W. Freude, and C. Koos, "Photonic wire bonding: a novel concept for chip-scale interconnects," Opt. Express **20**, 17667–17677 (2012).
127. M. R. Billah, M. Blaicher, T. Hoose, P.-I. Dietrich, P. Marin-Palomo, N. Lindenmann, A. Nesic, A. Hofmann, U. Troppenz, M. Moehrle, S. Randel, W. Freude, and C. Koos, "Hybrid integration of silicon photonics circuits and InP lasers by photonic wire bonding," Optica **5**, 876–883 (2018).
128. G. Giuliani, M. Norgia, S. Donati, and T. Bosch, "Laser diode self-mixing technique for sensing applications," J. Opt. A **4**, S283–S294 (2002).
129. M. Liess, G. Weijers, C. Heinks, A. van der Horst, A. Rommers, R. Duijve, and G. Mimnagh, "A miniaturized multidirectional optical motion sensor and input device based on laser self-mixing," Meas. Sci. Technol. **13**, 2001–2006 (2002).
130. A. Pruijmboom, M. Schemmann, J. Hellmig, J. Schutte, H. Moench, and J. Pankert, "VCSEL-based miniature laser-Doppler interferometer," Proc. SPIE **6908**, 69080I (2008).
131. D. Wiedenmann, M. Grabherr, R. Jäger, and R. King, "High volume production of single-mode VCSELs," Proc. SPIE **6132**, 613202 (2006).
132. M. Grabherr, R. King, R. Jäger, D. Wiedenmann, P. Gerlach, D. Duckeck, and C. Wimmer, "Volume production of polarization controlled single-mode VCSELs," Proc. SPIE **6908**, 690803 (2008).
133. M. Ortsiefer, M. Görblich, Y. Xu, E. Rönneberg, J. Rosskopf, R. Shau, and M.-C. Amann, "Polarization control in buried tunnel junction VCSELs using a birefringent semiconductor/dielectric subwavelength grating," IEEE Photon. Technol. Lett. **22**, 15–17 (2010).
134. P. Debernardi, J. M. Ostermann, M. Feneberg, C. Jalics, and R. Michalzik, "Reliable polarization control of VCSELs through monolithically integrated surface gratings: a comparative theoretical and experimental study," IEEE J. Sel. Top. Quantum Electron. **11**, 107–116 (2005).
135. D.-S. Song, Y.-J. Lee, H.-W. Choi, and Y.-H. Lee, "Polarization-controlled, single-transverse-mode, photonic-crystal, vertical-cavity, surface-emitting lasers," Appl. Phys. Lett. **82**, 3182–3184 (2003).
136. K.-H. Lee, J.-H. Baek, I.-K. Hwang, Y.-H. Lee, G.-H. Lee, J.-H. Ser, H.-D. Kim, and H.-E. Shin, "Square-lattice photonic-crystal vertical-cavity surface-emitting lasers," Opt. Express **12**, 4136–4143 (2004).
137. P. Debernardi, H. J. Unold, J. Maehnss, R. Michalzik, G. P. Bava, and K. J. Ebeling, "Single-mode, single-polarization VCSELs via

elliptical surface etching: experiments and theory," IEEE J. Sel. Top. Quantum Electron. **9**, 1394–1404 (2003).
138. T. Ohtoshi, T. Kuroda, A. Niwa, and S. Tsuji, "Dependence of optical gain in crystal orientation in surface-emitting lasers with strained quantum wells," Appl. Phys. Lett. **65**, 1886–1887 (1994).
139. K. Tateno, Y. Ohiso, C. Amano, A. Wakatsuki, and T. Kurokawa, "Growth of vertical-cavity surface-emitting laser structures on GaAs (311)B substrates by metalorganic chemical vapor deposition," Appl. Phys. Lett. **70**, 3395–3397 (1997).
140. O. Tadanaga, K. Tateno, H. Uenohara, T. Kagawa, and C. Amano, "An 850-nm InAlGaAs strained quantum-well vertical-cavity surface-emitting laser grown on GaAs (311)B substrate with high-polarization stability," IEEE Photon. Technol. Lett. **12**, 942–944 (2000).
141. K. D. Choquette and R. E. Leibenguth, "Control of vertical-cavity laser polarization with anisotropic transverse cavity geometries," IEEE Photon. Technol. Lett. **6**, 40–42 (1994).
142. B. Weigl, M. Grabherr, C. Jung, R. Jäger, G. Reiner, R. Michalzik, D. Sowada, and K. J. Ebeling, "High-performance oxide-confined GaAs VCSEL's," IEEE J. Sel. Top. Quantum Electron. **3**, 409–415 (1997).
143. P. Dowd, P. J. Heard, J. A. Nicholson, L. Raddatz, I. H. White, R. V. Penty, J. C. C. Day, G. C. Allen, S. W. Corzine, and M. R. T. Tan, "Complete polarisation control of GaAs gain-guided top-surface emitting vertical cavity lasers," Electron. Lett. **33**, 1315–1317 (1997).
144. H. Moench, M. Carpaij, P. Gerlach, S. Gronenborn, R. Gudde, J. Hellmig, J. Kolb, and A. van der Lee, "VCSEL based sensors for distance and velocity," Proc. SPIE **9766**, 97660A (2016).
145. L. A. Graham, H. Chen, J. Cruel, J. Guenter, B. Hawkins, B. Hawthorne, D. Q. Kelly, A. Melgar, M. Martinez, E. Shaw, and J. A. Tatum, "High power VCSEL arrays for consumer electronics," Proc. SPIE **9381**, 93810A (2015).
146. https://www.finisar.com/sites/default/files/downloads/application_note_vcsels_in_various_sensor_applications.pdf.
147. G. Berkovic and E. Shafir, "Optical methods for distance and displacement measurements," Adv. Opt. Photon. **4**, 441–471 (2012).
148. M.-C. Amann, T. Bosch, M. Lescure, R. Myllylä, and M. Rioux, "Laser ranging: a critical review of usual techniques for distance measurement," Opt. Eng. **40**, 10–19 (2001).
149. H. Moench, S. Gronenborn, X. Gu, R. Gudde, M. Herper, J. Kolb, M. Miller, M. Smeets, and A. Weigl, "VCSELs in short-pulse operation for time-of-flight applications," Proc. SPIE **10552**, 105520G (2018).
150. https://www.finisar.com/sites/default/files/downloads/application_note_pulsed_operation_of_vcsels_for_high_peak_powers.pdf.
151. R. Myllylä, J. Marszalec, J. Kostamovaara, A. Mäntyniemi, and G.-J. Ulbrich, "Imaging distance measurements using TOF lidar," J. Opt. **29**, 188–193 (1998).
152. M. E. Warren, D. Podva, P. Dacha, M. K. Block, C. J. Helms, J. Maynard, and R. F. Carson, "Low-divergence high-power VCSEL arrays for lidar application," Proc. SPIE **10552**, 105520E (2018).
153. J. Geng, "Structured-light 3D surface imaging: a tutorial," Adv. Opt. Photon. **3**, 128–160 (2011).
154. P. Qiao, W. Yang, and C. J. Chang-Hasnain, "Recent advances in high-contrast metastructures, metasurfaces, and photonic crystals," Adv. Opt. Photon. **10**, 180–245 (2018).
155. W. Zhou, D. Zhao, Y.-C. Shuai, H. Yang, S. Chuwongin, A. Chadha, J.-H. Seo, K. X. Wang, V. Liu, Z. Ma, and S. Fan, "Progress in 2D photonic crystal Fano resonance photonics," Prog. Quantum Electron. **38**, 1–74 (2014).
156. C. F. R. Mateus, M. C. Y. Huang, L. Chen, C. J. Chang-Hasnain, and Y. Suzuki, "Broad-band mirror (1.12–1.62 μm) using a subwavelength grating," IEEE Photon. Technol. Lett. **16**, 1676–1678 (2004).
157. S. Boutami, B. Ben Bakir, J.-L. Leclercq, X. Letartre, P. Rojo-Romeo, M. Garrigues, P. Viktorovitch, I. Sagnes, L. Legratiet, and M. Strassner, "Highly selective and compact tunable MOEMS photonic crystal Fabry–Perot filter," Opt. Express **14**, 3129–3137 (2006).
158. R. Magnusson and M. Shokooh-Saremi, "Physical basis for wideband resonant reflectors," Opt. Express **16**, 3456–3462 (2008).
159. V. Karagodsky, F. G. Sedgwick, and C. J. Chang-Hasnain, "Theoretical analysis of subwavelength high contrast grating reflectors," Opt. Express **18**, 16973–16988 (2010).
160. M. C. Y. Huang, Y. Zhou, and C. J. Chang-Hasnain, "A surface-emitting laser incorporating a high-index-contrast subwavelength grating," Nat. Photonics **1**, 119–122 (2007).
161. S. Boutami, B. Benbakir, J.-L. Leclercq, and P. Viktorovitch, "Compact and polarization controlled 1.55 μm vertical-cavity surface emitting laser using single-layer photonic crystal mirror," Appl. Phys. Lett. **91**, 071105 (2007).
162. T. Ansbæk, I.-S. Chung, E. S. Semenova, and K. Yvind, "1060-nm tunable monolithic high index contrast subwavelength grating VCSEL," IEEE Photon. Technol. Lett., **25**, 365–367 (2013).
163. S. Inoue, J. Kashino, A. Matsutani, H. Ohtsuki, T. Miyashita, and F. Koyama, "Highly angular dependent high-contrast grating mirror and its application for transverse-mode control of VCSELs," Jpn. J. Appl. Phys. **53**, 090306 (2014).
164. M. G. Moharam and T. K. Gaylord, "Rigorous coupled-wave analysis of planar grating diffraction," J. Opt. Soc. Am. **71**, 811–818 (1981).
165. M. C. Y. Huang, Y. Zhou, and C. J. Chang-Hasnain, "Single mode high-contrast subwavelength grating vertical cavity surface emitting lasers," Appl. Phys. Lett. **92**, 171108 (2008).
166. A. Liu, W. Hofmann, and D. Bimberg, "Two dimensional analysis of finite size high-contrast gratings for applications in VCSELs," Opt. Express **22**, 11804–11811 (2014).
167. A. Liu, W. Hofmann, and D. Bimberg, "Integrated high-contrast-grating optical sensor using guided mode," IEEE J. Quantum Electron. **51**, 6600108 (2015).
168. A. Liu, W. Zheng, and D. Bimberg, "Unidirectional transmission in finite-size high-contrast gratings," in *Asia Communications and Photonics Conference* (2016), paper AF2A.52.
169. D. Zhao, Z. Ma, and W. Zhou, "Field penetrations in photonic crystal Fano reflectors," Opt. Express **18**, 14152–14158 (2010).
170. I.-S. Chung and J. Mørk, "Speed enhancement in VCSELs employing grating mirrors," Proc. SPIE **8633**, 863308 (2013).
171. S. Goeman, S. Boons, B. Dhoedt, K. Vandeputte, K. Caekebeke, P. Van Daele, and R. Baets, "First demonstration of highly reflective and highly polarization selective diffraction gratings (GIRO-gratings) for long-wavelength VCSEL's," IEEE Photon. Technol. Lett. **10**, 1205–1207 (1998).
172. R. Magnusson, "Wideband reflectors with zero-contrast gratings," Opt. Lett. **39**, 4337–4340 (2014).
173. J. Lee, S. Ahn, H. Chang, J. Kim, Y. Park, and H. Jeon, "Polarization-dependent GaN surface grating reflector for short wavelength applications," Opt. Express **17**, 22535–22542 (2009).
174. M. Gębski, M. Dems, A. Szerling, M. Motyka, L. Marona, R. Kruszka, D. Urbańczyk, M. Walczakowski, N. Pałka, A. Wójcik-Jedlińska, Q. J. Wang, D. H. Zhang, M. Bugajski, M. Wasiak, and T. Czyszanowski, "Monolithic high-index contrast grating: a material independent high-reflectance VCSEL mirror," Opt. Express **23**, 11674–11686 (2015).
175. A. Liu, W. Zheng, and D. Bimberg, "Comparison between high- and zero-contrast gratings as VCSEL mirrors," Opt. Commun. **389**, 35–41 (2017).
176. W. Hofmann, C. Chase, M. Müller, Y. Rao, C. Grasse, G. Böhm, M.-C. Amann, and C. J. Chang-Hasnain, "Long-wavelength high-contrast grating vertical-cavity surface-emitting laser," IEEE Photon. J. **2**, 415–422 (2010).
177. K. Li, Y. Rao, C. Chase, W. Yang, and C. J. Chang-Hasnain, "Monolithic high-contrast metastructure for beam-shaping VCSELs," Optica **5**, 10–13 (2018).
178. P. Debernardi, R. Orta, T. Gründl, and M.-C. Amann, "3-D vectorial optical model for high-contrast grating vertical-cavity surface-emitting lasers," IEEE J. Quantum Electron. **49**, 137–145 (2013).
179. A. Liu, F. Fu, Y. Wang, B. Jiang, and W. Zheng, "Polarization-insensitive subwavelength grating reflector based on a semiconductor-insulator-metal structure," Opt. Express **20**, 14991–15000 (2012).
180. M. C. Y. Huang, Y. Zhou, and C. J. Chang-Hasnain, "A nanoelectromechanical tunable laser," Nat. Photonics **2**, 180–184 (2008).
181. Y. Rao, W. Yang, C. Chase, M. C. Y. Huang, D. P. Worland, S. Khaleghi, M. R. Chitgarha, M. Ziyadi, A. E. Willner, and C. J. Chang-Hasnain, "Long-wavelength VCSEL using high-contrast grating," IEEE J. Sel. Top. Quantum Electron. **19**, 1701311 (2013).
182. V. Karagodsky, B. Pesala, C. Chase, W. Hofmann, F. Koyama, and C. J. Chang-Hasnain, "Monolithically integrated multi-wavelength

VCSEL arrays using high-contrast gratings," Opt. Express **18**, 694–699 (2010).
183. C. Sciancalepore, B. B. Bakir, S. Menezo, X. Letartre, D. Bordel, and P. Viktorovitch, "III-V-on-Si photonic crystal vertical-cavity surface-emitting laser arrays for wavelength division multiplexing," IEEE Photon. Technol. Lett. **25**, 1111–1113 (2013).
184. A. Liu, P. Wolf, J.-H. Schulze, and D. Bimberg, "Fabrication and characterization of integrable GaAs-based high-contrast grating reflector and Fabry–Pérot filter array with GaInP sacrificial layer," IEEE Photon. J. **8**, 2700509 (2016).
185. A. Liu, W. Zheng, and D. Bimberg, "VCSEL with finite-size high-contrast metastructure," Proc. SPIE **10812**, 1081202 (2018).
186. E. Haglund, J. S. Gustavsson, J. Bengtsson, Å. Haglund, A. Larsson, D. Fattal, W. Sorin, and M. Tan, "Demonstration of post-growth wavelength setting of VCSELs using high-contrast gratings," Opt. Express **24**, 1999–2005 (2016).
187. L. Ferrier, P. Rojo Romeo, X. Letartre, E. Drouard, and P. Viktorovitch, "3D integration of photonic crystal devices: vertical coupling with a silicon waveguide," Opt. Express **18**, 16162–16174 (2010).
188. J. Ferrara, W. Yang, L. Zhu, P. Qiao, and C. J. Chang-Hasnain, "Heterogeneously integrated long-wavelength VCSEL using silicon high contrast grating on an SOI substrate," Opt. Express **23**, 2512–2523 (2015).
189. I.-S. Chung and J. Mørk, "Silicon-photonics light source realized by III-V/Si-grating-mirror laser," Appl. Phys. Lett. **97**, 151113 (2010).
190. G. C. Park, W. Xue, A. Taghizadeh, E. Semenova, K. Yvind, J. Mørk, and I.-S. Chung, "Hybrid vertical-cavity laser with lateral emission into a silicon waveguide," Laser Photon. Rev. **9**, L11–L15 (2015).
191. G. C. Park, W. Xue, M. Piels, D. Zibar, J. Mørk, E. Semenova, and I.-S. Chung, "Ultrahigh-speed Si-integrated on-chip laser with tailored dynamic characteristics," Sci. Rep. **6**, 38801 (2016).
192. S. Kumari, E. P. Haglund, J. S. Gustavsson, A. Larsson, G. Roelkens, and R. G. Baets, "Vertical-cavity silicon-integrated laser with in-plane waveguide emission at 850 nm," Laser Photon. Rev. **12**, 1700206 (2018).
193. M. Gębski, T. Czyszanowski, and J. A. Lott, "Electrically-injected VCSELs with a composite monolithic high contrast grating and distributed Bragg reflector coupling mirror," in *IEEE International Semiconductor Laser Conference (ISLC)* (2018), paper TuP38.
194. N. N. Ledentsov, V. A. Shchukin, V. P. Kalosha, N. N. Ledentsov, Jr., J.-R. Kropp, M. Agustin, Ł. Chorchos, G. Stępniak, J. P. Turkiewicz, and J.-W. Shi, "Anti-waveguiding vertical-cavity surface-emitting laser at 850 nm: from concept to advances in high-speed data transmission," Opt. Express **26**, 445–453 (2018).
195. G. Stepniak, A. Lewandowski, J. R. Kropp, N. N. Ledentsov, V. A. Shchukin, N. Ledentsov, Jr., G. Schaefer, M. Agustin, and J. P. Turkiewicz, "54 Gbit/s OOK transmission using single-mode VCSEL up to 2.2 km MMF," Electron. Lett. **52**, 633–635 (2016).
196. A. Liu, M. Xing, H. Qu, W. Chen, W. Zhou, and W. Zheng, "Reduced divergence angle of photonic crystal vertical-cavity surface-emitting laser," Appl. Phys. Lett. **94**, 191105 (2009).
197. A. J. Liu, W. Chen, H. W. Qu, B. Jiang, W. J. Zhou, M. X. Xing, and W. H. Zheng, "Single-mode holey vertical-cavity surface-emitting laser with ultra-narrow beam divergence," Laser Phys. Lett. **7**, 213–217 (2010).
198. A.-J. Liu, W. Chen, W.-J. Zhou, B. Jiang, F. Fu, H.-W. Qu, and W.-H. Zheng, "Squeeze effect and coherent coupling behaviour in photonic crystal vertical-cavity surface-emitting lasers," J. Phys. D **44**, 115104 (2011).
199. R. Puerta, M. Agustin, Ł. Chorchos, J. Tońska, J. R. Kropp, N. Ledentsov, Jr., V. A. Shchukin, N. N. Ledentsov, R. Henker, I. T. Monroy, J. J. V. Olmos, and J. P. Turkiewicz, "Effective 100 Gb/s IM/DD 850-nm multi- and single-mode VCSEL transmission through OM4 MMF," J. Lightwave Technol. **35**, 423–429 (2017).
200. I.-C. Lu, C.-C. Wei, H.-Y. Chen, K.-Z. Chen, C.-H. Huang, K.-L. Chi, J.-W. Shi, F.-I. Lai, D.-H. Hsieh, H.-C. Kuo, W. Lin, S.-W. Chiu, and J. Chen, "Very high bit-rate distance product using high-power single-mode 850-nm VCSEL with discrete multitone modulation formats through OM4 multimode fiber," IEEE J. Sel. Top. Quantum Electron. **21**, 444–452 (2015).
201. H. Li, D. B. Phillips, X. Wang, Y.-L. D. Ho, L. Chen, X. Zhou, J. Zhu, S. Yu, and X. Cai, "Orbital angular momentum vertical-cavity surface-emitting lasers," Optica **2**, 547–552 (2015).
202. S. Knappe, V. Shah, P. D. D. Schwindt, L. Hollberg, J. Kitching, L.-A. Liew, and J. Moreland, "A microfabricated atomic clock," Appl. Phys. Lett. **85**, 1460–1462 (2004).